Journal of Energy Storage 153 (2026) 121114

Contents lists available at ScienceDirect

Journal of Energy Storage

journal homepage: www.elsevier.com/locate/est

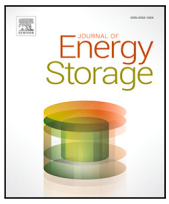

Research papers

Thermo-economic optimization of an adiabatic compressed air energy storage system including system dynamics

D. Pérez-Gallego [a,b,*], J. Gonzalez-Ayala [a,b], A. Medina [a,b], S. Anvari [a], I. Calderón-Vásquez [c], J.M. Cardemil [c], A. Calvo Hernández [a,b]

[a] Universidad de Salamanca, Department of Applied Physics, Salamanca, 37008, Castilla y Leon, Spain
[b] Universidad de Salamanca, Institute of Physics and Mathematics (IUFFYM), Salamanca, 37008, Castilla y Leon, Spain
[c] Pontificia Universidad Católica de Chile, Department of Mechanical and Metallurgical Engineering, Escuela de Ingeniería, Santiago, Chile

ARTICLE INFO

Keywords:
Thermo-mechanical energy storage
Adiabatic compressed air energy storage
Radial packed-bed systems
Dynamical integrated model
Multi-objective optimization
Thermo-economic objective functions

ABSTRACT

Adiabatic compressed air energy storage is a promising, in-development technology for storing renewable energy, for instance, from wind parks or photovoltaic installations. This work presents a multi-objective thermoeconomic optimization analysis. It is based on a dynamic model of the plant's thermodynamic performance, in which the dynamics of the thermal energy storage (packed-bed type) and the charge and discharge processes of the air reservoir are solved in detail. A plant configuration, as determined from previous work in our group, with *a priori* good round-trip efficiencies (around 0.76–0.78), is considered the starting point. It encompasses two-stage compression and expansion trains, along with two radial packed-beds (utilizing either sensible or phase-change materials) to capitalize on the cooling between compression steps. In the developed optimization procedure, the levelized cost of storage (LCoS) and the total capital expenditure (CAPEX) are taken as key performance indicators. The decision variables include, among others, mass flows, thermal energy storage dimensions, maximum and minimum cavern pressures, and the symmetry of the pressure ratios between compressors and turbines. The optimization procedure uses an NSGA-II genetic algorithm. One of the main novelties of the work is that accurate dynamic simulations have been used to obtain Pareto fronts. They are analyzed from different perspectives: the size, geometry, and materials of the packed-beds; the type of compressor (axial or centrifugal); energetic factors such as input and output energy and power; the maximum pressures in the cavern; and the mass flows in the charge and discharge processes. Values of LCoS are calculated with precision using realistic input data, resulting in approximately 80 €/MWh for a plant capable of storing 600 MWh (reference power of 200 MW for charge periods of 3 h) and electricity prices during charge of 50 €/MWh. The specific parameters and configurations that lead to those LCoS levels are made explicit. Furthermore, the influence of cavern costs, charging electricity prices, and idle time is analyzed in detail.

1. Introduction

Promoting energy storage (ES) is a key action in the European Union's 2030 Climate and Energy Strategy. This strategy aims to achieve a 40% reduction in greenhouse gas emissions relative to 1990 levels. The Paris Agreement similarly targets a net-zero emissions energy system by 2050 [1]. Furthermore, although fossil fuels remain dominant, essential renewable energy sources are experiencing continuous growth [2]. This growth could help achieve the Sustainable Development Goals adopted by the United Nations in 2015 [3]. It could also address the problem associated with grid management due to the difficulty of matching electricity generated from renewable sources with electricity demand [4,5].

In an energy storage (ES) facility, energy is usually stored during low-demand periods and released during peak-demand hours at the daily, weekly, or seasonal level. It is in this balance between continuous supply and demand that ES systems play a fundamental role, improving the performance of the power grid by controlling frequency, upgrading transmission line capacity, mitigating voltage fluctuations, and enhancing power quality and reliability. In short, ES increases the flexibility of how electricity is generated, delivered, and consumed, thus making power networks more resilient, efficient, and cleaner [6].

* Corresponding author.
E-mail address: dpgallego@usal.es (D. Pérez-Gallego).
URL: https://produccioncientifica.usal.es/investigadores/446328/detalle (D. Pérez-Gallego).

https://doi.org/10.1016/j.est.2026.121114
Received 19 December 2025; Received in revised form 10 February 2026; Accepted 15 February 2026

Nomenclature			
a_b	Ratio surface to volume of tank (m^{-1})	U	Effective heat loss coefficient (W/(m^2 K))
a_s	Surface area of particles per unit volume (m^{-1})	v	Interstitial velocity (m/s)
A_{cavern}	Internal area of the cavern (m^2)	V	Total volume of cavern (m^3)
AR	Packed-bed aspect ratio (-)	Greek letters	
C_{el}	Price of electricity for charge (€/MWh)	α	Convective heat transfer coefficient (W/(m^2 K))
c_p	Specific heat capacity (J/(kg K))	α_{eff}	Effective heat transfer coefficient (W/K)
D	Diameter of bed (m)	ϵ	Void fraction (–)
d_p	Diameter of bed particles (m)	η	Efficiency (–)
E	Energy (J)	λ_{lg}	Specific latent heat of vaporization (J/kg)
h	Specific enthalpy (J/kg)	μ	Dynamic viscosity (Pa s)
H	Packed-bed height (m)	ρ	Mass density (kg/m^3)
K	Thermal conductivity (W/(m K))	Subscripts	
LR	Layer ratio (–)	0	Nominal value
m	Total mass in the cavern (kg)	1cycle	One cycle
M	Molecular mass of air (kg/mol)	c	Charge
$\dot{m}_{\text{Red}}$	Reduced mass flow (–)	d	Discharge
$\dot{n}$	Reduced shaft speed (–)	eff	Effective
N	Plant lifetime (years)	f	Fluid
Nu	Nusselt number (–)	in	Input
p	Pressure (Pa)	max	Maximum
P	Power (W)	min	Minimum
$\dot{Q}$	Heat flow (W)	out	Output
r	Radius (m)	ref	Reference
$r_{\text{pc/pt}}$	Compressor/turbine pressure ratio (–)	s	Storage material
t	Time (s)	w	Cavern wall
T	Absolute temperature (K)	∞	Ambient
T_w/T_∞	Cavern wall/ambient temperature (K)		

Acronyms			
AACAES	Advanced Adiabatic-CAES	LCoE/S	Levelized cost of electricity/storage
ACAES	Adiabatic-CAES	LMTD	Logarithmic mean temperature difference
AEY	Annual energy yield	LP	Low pressure
A+C	Axial + centrifugal	LPC/LPT	Low-pressure compressor/turbine
BOP	Balance of plant	LRC	Lined-rock cavern
CAES	Compressed air energy storage	MILP	Mixed-integer linear programming
CAPEX	Capital expenditure	NSGA	Non-dominated sorting genetic algorithm
C+C	Centrifugal + centrifugal	OM	Operation and maintenance
CONT	Contingency	OPEX	Operational expenditure
CRF	Capital recovery factor	ORC	Organic Rankine cycle
EPC	Engineering, procurement, and construction	PB	Packed-bed
FDM	Finite difference method	PCM	Phase-change material
HE	Heat exchanger	PTES	Pumped thermal energy storage
HP	High pressure	RTE	Round-trip efficiency
HPC/HPT	High-pressure compressor/turbine	TES	Thermal energy storage
HTF	Heat transfer fluid	TIT	Turbine inlet temperature
KLD	Kullback–Leibler divergence	TRL	Technology readiness level
KPI	Key performance indicator		

Large-scale ES systems are necessary to accommodate excess off-peak energy generation and to deliver high power during peak load, allowing power plants to operate at their highest efficiency while also providing the required distribution and transmission flexibility. Thus, for long-term storage, large-scale energy storage is the only available solution to achieve appropriate grid management by integrating security and balancing supply and demand [4,7,8].

Among long-term thermo-mechanical storage solutions, Adiabatic Compressed Air Energy Storage (ACAES) remains one of the most promising technologies for large-scale electricity storage with renewable energy sources [9]. In a conventional ACAES plant, atmospheric air is compressed and stored under pressure, typically during periods of low demand or valley prices, in geological or engineered reservoirs. When electricity is needed, the pressurized air is reheated and expanded through a turbine. This generally occurs during peak demand periods and powers a generator to produce electricity without external fuels.

The compression train employs inter-coolers and after-coolers to reduce the temperature of the compressed air, with this heat collected in thermal energy storage (TES) units (for instance, packed-bed systems, PB). During expansion, stored air is withdrawn and reheated using the energy captured during compression. Therefore, ACAES technology reduces pollutant emissions, enhances efficiency, and lowers thermal stress on the storage enclosure. Optimizing these advantages demands robust ACAES plant configurations and suitable heat storage materials. Such measures support technological maturity relative to other

large-scale energy storage systems. At the present, the technological-readiness level (TRL) of ACAES is considered 4, comparable to the Pumped Thermal Energy Storage (PTES) concept, but below other thermo-mechanical storage systems, such as pumped hydro, diabatic CAES, and liquid air energy storage (LAES) [9]. Several implementations of various ACAES plants are documented in [10–12]. King et al. summarized in [13] several projects on CAES and the potential underground storage capacity in India and UK.

Together with the HP-store and the turbomachinery, the third crucial subsystem in an ACAES plant is the integrated thermal energy storage. This integration eliminates the need for external heat exchangers, which would otherwise cause additional energy and exergy losses. Two main concepts exist in this regard. Sensible heat storage is based on storing thermal energy by changing the temperature of the TES material, either in solid or liquid phase [14]. Latent heat storage utilizes the latent heat of phase-change materials (PCMs) during phase transitions, primarily between solid and liquid states [15]. Hybrid systems combining sensible and latent TES have also been surveyed [16]. An advanced concept incorporates various PCM materials in multi-layered or cascade packed-bed structures [17,18]. In all cases, the thermophysical properties of the materials and the geometry of the packed-bed play key roles in the overall performance of ACAES plants [19]. A pilot-scale advanced ACAES plant using a combination of sensible and latent TES was developed at ETH Zürich [20,21]. A third, much less common kind of TES material, is based on the thermochemical heat recuperation concept [22,23]. Here, energy is derived from chemical bonds, often through solid–gas reactions. The main advantage over sensible and latent systems is higher energy density.

However, and beyond the traditional thermodynamic methods based on energy and/or exergy analysis [23,24], the proposed purely thermodynamic designs for ACAES plants are not necessarily economically feasible, as economic aspects such as capital and/or operational costs are not considered. Techno-economic analysis plays a crucial role as a further step toward designing systems with reduced costs, ensuring both efficiency and economic viability. Additionally, these long-term techno-economic methods enable the evaluation of each system component's performance and the identification of critical components with the highest potential for system improvement in real grids with fluctuating renewable energy inputs [4]. Several research works have been devoted to the economic optimization of both isochoric and isobaric ACAES plants, working alone or integrated with cooling, heating, and power systems; see, for instance, Refs. [25–27].

In multi-objective optimization methods, several objectives are simultaneously optimized, and the best compromise among all of them is found by means of the so-called Pareto front [28]. In the exergoeconomic ones, the key performance indicators (KPI) are functions arising from the economic value of lost exergies and their minimization [29–31]. In purely economic schemes, typical KPIs include capital expenditure (CAPEX), levelized cost of storage (LCoS), and energy or power capital costs [32–35]. The latter can be mono-objective. Their aim is to minimize the costs of the bought electricity with Mixed-Integer Linear Programming (MILP) techniques or to maximize the difference between purchase and sales costs, *i.e.*, the economic profit. These mono-objective methods yield a single solution, rather than a Pareto front. In [32] Mersch et al. presented an optimization that accounts for a dynamic model of system operation with solid or liquid thermal stores. They used round-trip efficiency or energy capital cost as objective functions. The predicted energy/power capital costs and round-trip efficiencies were compared with those of other large-scale electrical energy storage technologies.

Comparing the expected LCoS of CAES or ACAES with other storage technologies is challenging, and several differing estimations can be found in the literature. Factors such as storage duration, number of cycles per year, charging electricity costs, round-trip efficiency, financing costs, site/geological particularities, and others make it uncertain to provide confidence intervals. The following lines briefly enumerate the conclusions of some studies.

- Viswanathan et al. [36] give an interval 89–160 €/MWh for diabatic CAES plants between 100 and 1000 MW, natural gas-fired, and 29 €/MWh electricity charging cost.
- In a report for the US Energy Agency, Ahmed et al. [37] give an indicative interval for ACAES plants between 134 and 535 €/MWh, but it is highlighted that these numbers are very tech- and site-dependent.
- From their own simulations, O. Schmidt [38] estimates a median LCoS value for CAES about 223 €/MWh.
- Smallbone et al. present in [39] the comparison among several energy storage technologies. For 100 MW/400 MWh plants with 365 cycles per year and assuming an electricity price of 30 €/MWh, their results give similar LCoS intervals for CAES and ACAES: 120–150 €/MWh (see Figs. 5 and 6 in [39]). These values for LCoS are higher than those for pumped hydro storage, 80–120 €/MWh. The foreseen values for pumped thermal energy storage (PHES) have a wider LCoS interval, approximately from 80 to 150 €/MWh. Li-ion batteries are expected by 2030 to have LCoS values between approximately 120–240 €/MWh and H_2 technologies between 180 and 260 €/MWh in comparable conditions.

In summary, low-end values (90–100 €/MWh) have to be taken with caution because they assume very favorable conditions (high cycle count, low charging cost, ideal site, etc.). High-end values, on the contrary (130–530 €/MWh), can be considered as cautionary upper bounds for less favorable conditions or early-stage ACAES.

A detailed analysis of several ACAES configurations by using a fully thermodynamic dynamic model for each component and their integration in an overall plant has been reported recently by us [40]. A symmetrically balanced arrangement with two compressors, two expanders, and two intermediate packed-bed thermal storage (PB-TES) systems was considered a good candidate for revealing general trends and achieving high overall performance, as the absorbed/released heat in the TES matches the cooling/heating processes after compression/expansion. The compression train was assumed to be formed by two centrifugal low- and high-pressure compressors operating under off-design conditions, at least one always following the maximum efficiency line by continually adjusting rotational speed and mass flow rate to avoid back-pressure effects in the high-pressure store. The expansion subsystem features a throttling valve to ensure a constant pressure in the discharge and two axial turbines with fixed pressure ratios. The PB-TES systems were simulated using recent designs based on a radial-flow, high-temperature system with low pressure drop. This work enabled full-time-dependent simulation of the effects of different devices or arrangements on round-trip efficiency and exergy metrics.

The primary objective of this paper is to conduct a comprehensive and optimized techno-economic assessment of an ACAES time-dependent model [40], taking into account the technical and economic characteristics of its components and the overall plant. The levelized cost of storage (LCoS) and capital expenditure (CAPEX) are considered as KPIs. The multi-objective optimization process is performed using an initial Monte Carlo procedure followed by a Non-Dominated Sorting Genetic Algorithm II (NSGA-II) implemented from scratch in Mathematica© to search for the Pareto optimal sets and the Pareto front for several variables. The analysis of the high-pressure store, the compression train, various TES materials, PBs size and geometry, and the impact of electricity prices on charging is specifically considered. The main novelties of this work could be briefly summarized as follows:

- A fully dynamic model on a thermodynamically efficient ACAES plant configuration is considered: the dynamics of the high-pressure reservoir are coupled to those of the packed-beds to realistically represent plant operation.
- The compression train, with two compressors in series, is analyzed in detail. It may include an axial and a centrifugal compressor, or two centrifugal compressors.

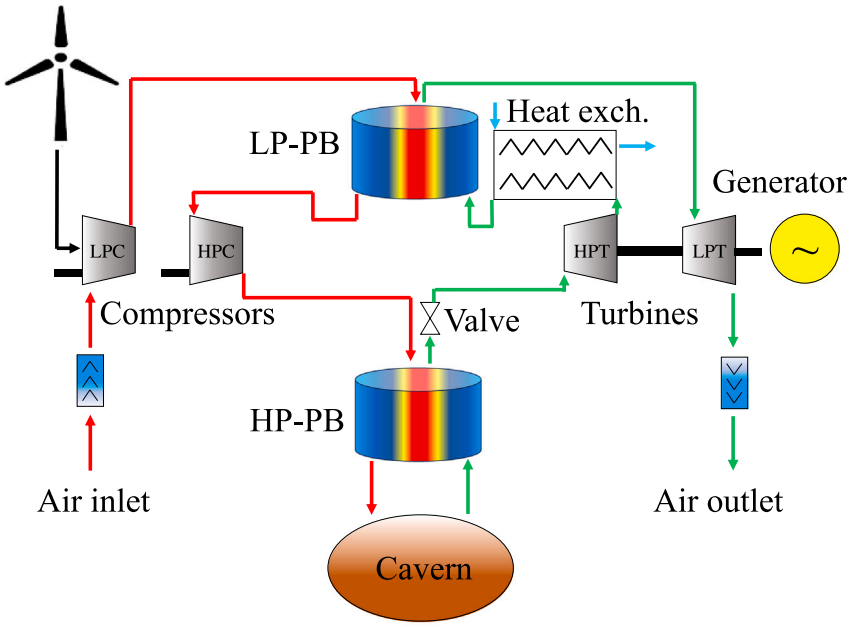

Fig. 1. Considered ACAES plant configuration. It is formed by two compressors in series (LPC and HPC) with packed-bed thermal storages at the exit of each one (LP-PB and HP-PB), a high-pressure air reservoir (cavern), two turbines for the expansion train (HPT and LPT), and a heat exchanger for avoiding the degradation of the thermocline of the low-pressure packed-bed.

- In the dynamic model, the NSGA-II algorithm is utilized to generate Pareto fronts for LCoS and CAPEX trade-offs. The impact of key parameters in the high-pressure reservoir, turbomachinery, and packed-bed thermal storage is analyzed. Also, optimization constraints and variable correlations are studied in depth.
- A complete economic analysis for several design options is presented, including the type of materials for the packed-beds (sensible or PCM); the costs of the cavern; charge, discharge, and storage times; and the input electricity price.

The paper is structured as follows. Section 2 provides a summary of the considered plant configuration and the arguments in favor of such a choice. The main methodological schemes considered for the modeling of plant subsystems and the thermo-economic framework are exposed in Section 3. Section 4 is devoted to explaining the numerical implementation and the validation of subsystems and the overall plant, and to introducing the decision variables with their boundaries and constraints for the multi-objective optimization process. In Section 5, the main results of the work are presented and discussed in detail. Finally, in Section 6, the most novel and relevant conclusions of the analysis are presented.

2. Plant configuration

In a recent publication [40], a comprehensive dynamic computational model was applied to analyze several ACAES plant configurations in depth. All configurations share a common element: a compression train for the charge phase, consisting of two compressors in series, and an expansion train, consisting of two turbines. Recent studies have highlighted that such a configuration with two-stage compression and expansion trains is a thermodynamically reasonable one for ACAES plants [18,32]. The referred study [40] moreover considered layouts with one or two packed-bed thermal storage units, each with axial or radial symmetry. The thermodynamic analysis showed that the most efficient configuration, in terms of round-trip efficiency (RTE), was the one depicted in Fig. 1. As shown in the figure, a low-pressure radial packed-bed (LP-PB) cools the air between the first and second compressors. The stored heat is recovered during discharge between the turbines. A second packed-bed (HP-PB), also radially symmetric, extracts heat from the air before it enters the storage cavity. This stored heat reheats air before the first turbine during discharge. A throttling valve at the HP-PB exit maintains a constant inlet pressure to the high-pressure turbine. In addition, a heat exchanger cools the working fluid at the exit of the first high-pressure turbine before it enters the LP-PB, thereby preventing thermocline degradation. In the design in [40], this heat exchanger is also connected to a bottoming organic Rankine cycle (ORC) to boost efficiency. However, for this optimization work, the ORC is not considered to simplify the analysis and interpretation of the operation variables.

It is also important to note that in [40] two kinds of compression trains were considered: the most usual one in previous ACAES configurations (a mixed one with an axial low-pressure compressor followed by a centrifugal high-pressure one) and a compression train formed by two similar centrifugal compressors. Additionally, this work will discuss both types of compression layouts. In the next section, the basic methodological elements for modeling each subsystem conforming the whole plant are presented.

3. Methodological elements

3.1. Plant subsystems

3.1.1. Turbomachinery

In general terms, axial compressors (machines that use rotating airfoils to increase air pressure) are cheaper than centrifugal compressors (machines that use a rotating impeller to increase air pressure by changing the direction of airflow). However, axial compressors operate within narrower mass flow and pressure ratio intervals. Thus, in most CAES plants with compression trains containing two compressors in series, the first low-pressure compressor (LPC), which takes in air at near atmospheric pressure, is selected as axial. The second, high-pressure compressor (HPC), is centrifugal because it works at a variable (high) outlet pressure as the air fills the storage cavity. This operation requires a pressure ratio that varies widely. The combination of both types of compressors rarely follows the line of maximum efficiency during the

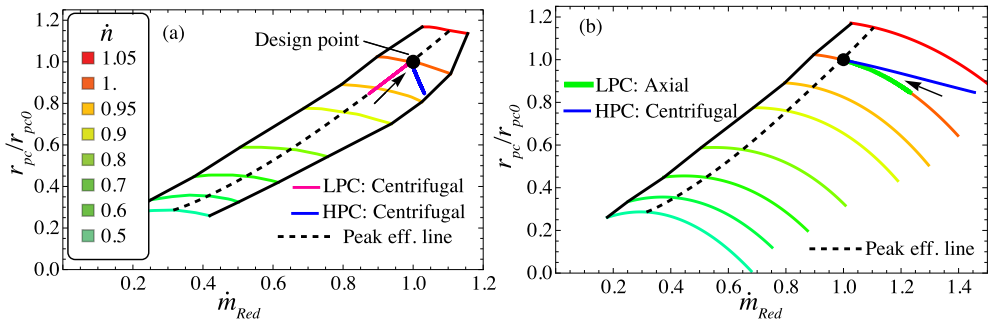

Fig. 2. Operational maps for the compressors during the charge phase: Reduced pressure ratios, r_{pc}/r_{pc0}, against reduced mass flows, $\dot{m}_{Red}$ for several rotational speeds, $\dot{n}$. (a) Configuration with two centrifugal compressors in series (C+C). (b) configuration with an axial LPC and a centrifugal HPC (A+C). Reduced variables are defined as in [41].

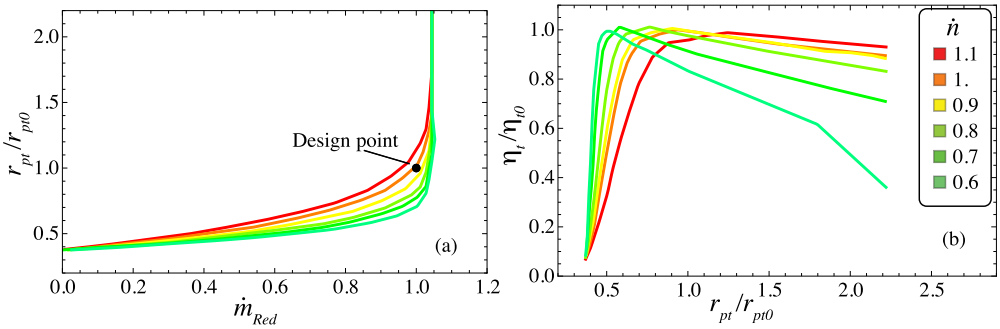

Fig. 3. Operational maps for the turbines [41]. (a) Reduced pressure ratio, r_{pt}/r_{pt0}, against reduced mass, $\dot{m}_{Red}$, for different rotational speeds, $\dot{n}$. (b) Reduced isentropic efficiency, η_t/η_{t0} as a function of the reduced pressure ratio.

charging process. For this reason, the option of using two centrifugal compressors in series is also analyzed in this work. This alternative may require a larger initial investment in the plant, but operation can be more efficient from the thermodynamic viewpoint. Therefore, it appears challenging to compare both options from a thermo-economic perspective.

The present model assumes that the pressure inside the isochoric air storage cavity increases during charging (see the next subsection). The evolution of the compression ratio varies the reduced mass with the compressor's rotational speed. Then, a trajectory in the operational map (taken from [41]) is fixed according to efficiency requirements. For the LPC, in the case that two centrifugal compressors are considered (C+C), the peak-efficiency line is chosen (see Fig. 2(a)). And when a mixed train, axial/centrifugal, is taken (A+C), the LPC trajectory is over a constant rotational speed leading to the peak efficiency (Fig. 2(b)). In any case, processes for LPC and HPC finish always at the design point (see both panels in Fig. 2). At the end of the charge step, the outlet pressure at the HPC should be slightly higher than in the cavern to avoid back-pressure effects.

The turbines considered for the expansion/discharge step are axial. During the expansion phase, the high-pressure turbine (HPT) receives air from the outlet of the HP-PB, where the pressure decreases over time (see Fig. 1). However, since the flow passes through the throttling valve (considered isenthalpic for modeling purposes), the pressure at the HPT inlet remains nearly constant. As a result, the inlet air to the HPT has a decreasing temperature (turbine inlet temperature, TIT), but an essentially constant pressure throughout the discharge. The mass flow is therefore adjusted to operate the turbine close to its design point (see Fig. 3). The second, low-pressure turbine (LPT), operates in a similar manner. The air at its inlet (entering from the LP-PB) exhibits a time-dependent (decreasing) temperature and an approximately constant pressure. In this work, the operational maps for the axial turbines developed in [41] were used through interpolation fitting.

3.1.2. High-pressure air reservoir

From a practical perspective, high-pressure air reservoirs for CAES systems could be either man-made pressure vessels or geologic structures [42]. The latter can be underground caverns such as salt cavities, confined aquifers, lined rock caverns (LRC), or depleted natural gas or petroleum deposits. They may be considered built if they are disused sites with basic impermeability, so they may not be too expensive. But they can also be taken as unbuilt if they require more extensive preparation. Built and unbuilt salt cavities and lined rock caverns will be considered in this work from an economic viewpoint.

From the thermodynamic perspective, isochoric high-pressure air storage is considered. It will be assumed that the varying mass of air inside the reservoir always behaves as an ideal gas, with changing pressure and temperature during charge and discharge processes. Air properties are considered temperature- and pressure-dependent. The cavern will not be considered adiabatic at any stage; a convective heat exchange between the stored air and its surroundings will be taken into account.

In the following paragraphs, the basic assumptions and differential equations arising from mass, and energy conservation, which are used to solve the dynamics of the compressed air storage, are briefly outlined. More details can be found in [40,43].

- Mass conservation: The time-dependent mass flow through cavity inlet and outlet is denoted $\dot{m}(t)$, and the subscripts c and d stand for charge and discharge periods. Thus,

$$\dot{m} = \dot{m}_c - \dot{m}_d. \tag{1}$$

- Energy conservation can be separated in terms associated to internal energy and enthalpy variations, and also to heat transfers through the cavity walls. In a descriptive form:

$$\overbrace{\frac{d(mu)}{dt}}^{\text{internal energy variations}} = \overbrace{\dot{m}_c h_{\text{in}}}^{\text{enthalpy incoming}} - \overbrace{\dot{m}_d h_{\text{out}}}^{\text{enthalpy outgoing}} - \overbrace{\alpha_{\text{amb}} A_{\text{cavern}} \left(T - T_w\right)}^{\text{heat transfer through the walls}} . \quad (2)$$

In this equation, A_{cavern} is the internal area of the storage cavity, and the air temperature therein at any time is $T(t)$. The convective heat transfer coefficient between the cavern and its surroundings is denoted as α_{amb}. T_w is the temperature of the cavern walls (that is, the ambient temperature). The specific internal energy is denoted with u. The specific enthalpies of the inlet or outlet fluid per unit mass, respectively, are h_{in} or h_{out}.

Using the equation of state of an ideal gas and considering that all processes are isochoric, energy conservation can be expressed in a more practical form as:

$$mc_p \frac{dT}{dt} - \frac{RT}{M}(\dot{m}_c - \dot{m}_d) - \frac{mR}{M}\frac{dT}{dt} = \dot{m}_c c_p (T_{\text{in}} - T) - \alpha_{\text{eff}} \left(T - T_w\right), \quad (3)$$

where M is air's molar mass, c_p air's specific constant-pressure heat, and R the ideal gas constant. For numerical implementation, the convective heat transfer between the air in the cavity and its surroundings is quantified by an effective coefficient, $\alpha_{\text{eff}} = V(0.2356 + 0.0149|\dot{m}_c - \dot{m}_d|^{0.8})$, following [43], where V is the total volume of the cavity.

This set of differential equations (for the mass of air inside the cavity and its temperature) are solved in time with an implicit Euler's method for finite difference problems (details can be found in [40]):

$$\frac{dm}{dt} = \frac{m^t - m^{t-1}}{\Delta t}; \qquad \frac{dT}{dt} = \frac{T^t - T^{t-1}}{\Delta t}. \quad (4)$$

3.1.3. Packed-bed thermal energy storage

In the ACAES system studied, two packed-bed thermal energy storage units are used to store heat: one between compressors (LP-PB) and another after the second compressor (HP-PB), before the air enters the storage cavity during the charge mode (see Fig. 1). In discharge mode, this stored energy increases the inlet temperatures of both turbines, allowing for more efficient power production and reducing low-temperature undesired effects. Packed-bed stores enable direct thermal contact between the air working fluid and the heat-storing material, thereby avoiding the high exergy losses associated with external heat exchangers (HEXs) that use indirect contact. This direct contact is closer to reversible conditions because both cooling and heating occur in the same device. PB-TES are considered highly effective for heat storage compared to HEX-TES systems [44,45].

Considering its geometrical symmetry, two types of PB systems can be distinguished: axial or radial. The second ones, recently analyzed by Trevisan et al. [46] numerically and experimentally, have the advantage (among other technical ones) of lower pressure decays. In the standard cylindrical axial ones, the HTF flows along the axial direction of the cylinder. Pressure drops are proportional to cylinder length. Nevertheless, in radial PBs (see Fig. 4) for instance during the charge step, the HTF enters through a central pipe and is radially distributed across the particles in all directions. The HTF is collected after the heat transfer to the solid particles by a perimetric annulus and then conducted to the top of the tank. During discharge flow directions are reversed. Therefore, pressure decays are not homogeneous; they are larger closer to the cylinder axis, where the fluid velocity is higher. If larger-sized particles are located in this region, with more interstitial room for the fluid to flow among them, pressure decay is smaller. A second layer of smaller particles (separated from the largest ones with a fine wire mesh), or even more layers of decaying-sized particles, can be included near the cylinder walls. This provides a larger contact area, which benefits heat transfer. McTigue and White [47] have also analyzed radial packed-beds for thermal storage applications, concluding that they have similar efficiencies to the axial ones and are competitive from a thermo-economic viewpoint. Radial packed-beds lead to steeper thermoclines, which can induce more convective losses, but they favor larger mass flows for higher charge and discharge speeds. This point is especially interesting for ACAES systems.

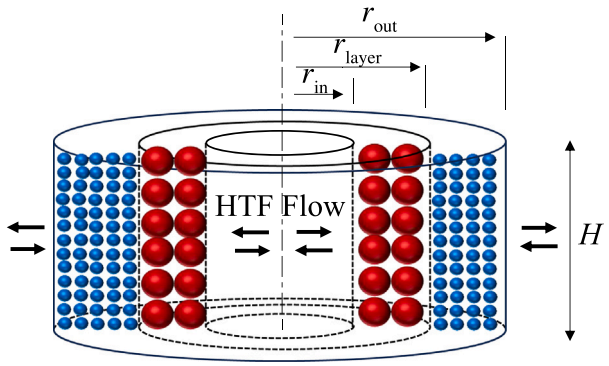

Fig. 4. Schematic representation of the considered radial packed-bed thermal storage system. The aspect ratio coefficient is defined as, $AR = r_{\text{out}} - r_{\text{in}}/H$.

Pressure drops for both types of PB units were explicitly calculated in [40] for an ACAES configuration similar to that considered in this work. For the low-pressure two-layer radial PB (LP R-PB), a decrease in the pressure drop of 22.5% with respect to the axial geometry was found at the end of the charge phase. A similar difference, favorable to the radial configuration, was estimated for the discharge phase. This decrease in the pressure drops for radial PBs directly impacts ACAES round-trip efficiency (RTE). In Ref. [40](see Fig. 23), the RTE for a configuration including a bottoming ORC between expansion turbines reached 0.79 at the stationary state (after 30 cycles). In consequence, a two-layer radial PB layout is considered in this work for all computations.

A key parameter for defining the geometry of radial PBs is the layer ratio, $LR = (r_{\text{layer}} - r_{\text{in}})/(r_{\text{out}} - r_{\text{in}})$ (see Fig. 4 for the notation). It will be considered as an optimization variable in the following sections.

The dynamics of the radial PB units are solved by conforming a system of differential equations arising from mass, energy, and momentum conservation. These equations were thoroughly analyzed in previous works [40,48], so a brief summary is provided next.

- Mass conservation:

$$\frac{\partial \rho_f}{\partial t} + \nabla(v\rho_f) = 0, \quad (5)$$

In this equation and in the following ones, the subindex f stands for fluid (in this work air) and s for solid. ρ_f is the fluid density, A the cross section of the PB cylinder, $v = \dot{m}/(\epsilon \rho_f A)$ is the fluid velocity, and ϵ the void fraction, that is considered the same for the two layers provided that it is assumed that the volume of the tank is much larger than that of the spherical particles.

- Energy conservation:

$$\epsilon \rho_f c_{p,f} \left(\frac{\partial T_f}{\partial t} + v\frac{\partial T_f}{\partial r}\right) = K_{\text{f,eff}} \frac{1}{r}\frac{\partial}{\partial r}\left(r\frac{\partial T_f}{\partial r}\right) + \alpha a_s \left(T_s - T_f\right) + U a_b \left(T_\infty - T_f\right), \quad (6)$$

$$(1-\epsilon)\rho_s c_{p,s} \left(\frac{\partial T_s}{\partial t}\right) = K_{\text{s,eff}} \frac{1}{r}\frac{\partial}{\partial r}\left(r\frac{\partial T_s}{\partial r}\right) + \alpha a_s \left(T_f - T_s\right). \quad (7)$$

These equations, for the fluid and the solid, come from considering a continuous solid phase model [49] with the particularity of

taking cylindrical coordinates: r refers to the radial distance. The first term of both equations arise from enthalpies variations.

The convective heat transfer between the solid and the fluid is quantified through $\alpha = (K_f.N_u)/d_p$ where: K_f is the fluid thermal conductivity, N_u the Nusselt number, and d_p the particles diameter for each layer. The surface area of the solid per unit volume is $a_s = 6(1-\epsilon)/d_p$. The effective conductivities $K_{f,eff}$ and $K_{s,eff}$ measure thermal conduction in the fluid and the solid respectively (in the radial direction).

The heat leak from the cylinder inner to its surroundings is computed through an effective parameter U (second term of Eq. (6)). a_b represents the ratio between the internal surface and the total volume and T_∞ the surroundings temperature. For a radial PB, $a_b = 1/H$, where H is the total cylinder length.

Mass and energy conservation equations are solved by means of an implicit Euler's method (details in [40,48]).

- Momentum conservation can be introduced in the form of a relationship for the pressure decay (in the radial direction in this case). Ergun's formula for monodispersed spherical particles and uniform porosity, the Ergun's formula is considered [50]:

$$\frac{-\Delta p}{L} = 150\frac{(1-\epsilon)^2}{\epsilon^3}\frac{\mu_f}{d_p^2}v + 1.75\frac{(1-\epsilon)}{\epsilon^3}\frac{\rho_f}{d_p}v^2, \tag{8}$$

where μ_f is the dynamic viscosity of the fluid. In a radial packed-bed $L = r_{out} - r_{in}$, and the cross-section $A = 2\pi rH$.

All the parameters required to solve this system of differential equations and the pressure decay will be made explicit below.

3.1.4. Heat exchanger

A heat exchanger between the outlet of the first high-pressure turbine and the low-pressure packed-bed (see Fig. 1) is used to decrease the temperature of the air flowing inside the LP packed-bed (close to ambient temperature) to prevent the degradation of the thermocline in that packed-bed. From an energetic viewpoint, it would be more interesting to couple a bottoming Rankine cycle capable of operating at the HP turbine outlet temperature. This fact was analyzed in [40]. Although the configuration with a bottoming ORC increases the RTE of the whole plant by a few points, for the optimization objectives of this work, it was discarded for practical reasons: the complexity of the entanglement among subsystem variables and the considerably higher computation times. The exchange surface area of the heat exchanger is calculated using the LMTD method.

3.2. Key thermo-economic indicators

The objective of this work is to perform a complete thermo-economic optimization based on a plant layout that was previously analyzed and pre-optimized in terms of energetic and exergetic criteria [40]. The key performance indicators to be simultaneously considered are the capital expenditure (CAPEX) and the levelized cost of storage (LCoS). The latter represents the minimum average price at which the produced electricity should be sold for amortizing all expenditures during the whole operation time of the plant, typically 30 years. The LCoS is defined in terms of four key parameters: the CAPEX itself, the capital recovery factor (CRF), the operational expenditure (OPEX), and the annual energy yield (AEY). The latter is directly related to the round-trip efficiency of the plant (RTE), RTE=E_{out}/E_{in} [33,51,52]. Thus, the RTE could be considered as a supportive performance indicator.

$$LCoS = (CAPEX \cdot CRF + OPEX)/AEY. \tag{9}$$

The CAPEX can be expressed as:

$$CAPEX = C_{land} + (C_{site} + C_{equipment} + C_{BOP}) \cdot (1 + f_{CONT})(1 + f_{EPC}), \tag{10}$$

where:

- C_{land} represents the purchase cost of the land where the plant will be built.
- C_{site} is the cost associated to the civil works required to make the land usable for plant construction and operation.
- $C_{equipment}$ is the cost of all the required (core technology) equipment.
- C_{BOP} is the cost of the balance of the plant (all the components that are necessary but not directly related to the basic plant technology, as electrical infrastructure, control and auxiliary systems, etc.).
- f_{CONT} is a contingency factor accounting for uncertainties, risks, and unforeseen payments.
- f_{EPC} is the factor that measures engineering, procurement, and construction costs (design studies, system integration, quality assurance, labor management, logistics, profit margin, risk premium, etc.).

Inflation is estimated with Marshall and Swift index [53]. Balance of plant costs, C_{BOP}, are considered as: $C_{BOP} = c_{BOP} \cdot P_{gross}$ and $P_{gross} = 1.05 \cdot P_{out,net}$. For the ACAES plant under consideration, equipment costs can be split in the following way (see Fig. 1):

$$C_{equipment} = C_{LPC} + C_{HPC} + C_{LPT} + C_{HPT} + C_{cavern} + C_{generator} + C_{HP\text{-}PB} + C_{LP\text{-}PB} + C_{HE} + C_{piping}. \tag{11}$$

Correlations and sources for all these terms are explicit in Appendix A.1. The cost of the throttling valve is disregarded.

A particularly difficult term to estimate in the ACAES plant is that corresponding to the high-pressure cavity or cavern where air is stored. C_{cavern} includes the costs of the site itself, preparation, and making it airtight. Initial preparation costs may include geophysical exploration, well drilling, salt cavern leaching, mattress gas injection, lining and sealing, and surface infrastructure for control. Although lined rock caverns are more expensive than, for instance, salt caverns, thermal energy deposits do not require an extensive mechanical insulation because they can be located inside the cavern to avoid large pressure gradients. For instance, the construction cost for a $3 \cdot 10^5$ m^3 lined rock cavern is about 106 mill. € (see data in [42] and the Appendix). The construction cost for a salt cavern of the same volume is 32.5 mill. €. Specific cost data are available in Appendix A.2 for the geologic sites considered in this work: built or unbuilt LRC or salt caverns.

Different TES materials will be analyzed in this work, including sensible and latent (PCM) materials. The Appendix contains a list (Table A.9) with the physical properties and specific prices of the materials that have been surveyed to estimate $C_{HP\text{-}PB}$ and $C_{LP\text{-}PB}$.

The capital recovery factor is calculated as:

$$CRF = \frac{r(1+r)^N}{(1+r)^N + 1}, \tag{12}$$

where r is the real discount rate, calculated from the nominal discount, d, and the interest rate, i: $r = (1+d)/(1+i) - 1$ with $d = 7\%$ and $i = 2.5\%$ (see [33] and references therein). The lifetime of the plant, N, is assumed to be 30 years.

The OPEX includes all the operation and maintenance costs of the plant. Particularly, three terms are considered [4,54]: a fixed costs term, proportional to the nominal power output of the plant, a second one proportional to the annual energy yield (AEY) or total energy out, and another one associated to the price at which electricity is bought during the charging periods.

$$OPEX = C_{OM,fix} \cdot P_{out,net} + C_{OM,prod} \cdot AEY + C_{el} \cdot E_{charging}. \tag{13}$$

The grid fees are not considered in the OPEX because they present a great uncertainty depending on the regulations of each country, the connection of the plant to the grid, the power levels, the operation of the grid, and other factors.

The annual electricity yield, AEY, and the total energy bought in a year, $E_{charging}$, can be calculated as:

$$AEY = \frac{365 \cdot 24}{t_{charge} + t_{discharge} + t_{idle}} E_{out,1cycle}, \quad (14)$$

$$E_{charging} = \frac{365 \cdot 24}{t_{charge} + t_{discharge} + t_{idle}} E_{in,1cycle}, \quad (15)$$

where $E_{out,1cycle}$ and $E_{in,1cycle}$ are the energy produced in each discharge cycle and consumed for each charge cycle, respectively.

3.3. Optimization procedure

The multi-objective optimization process can be performed using different methodologies. Initially, a Monte Carlo procedure was used, but due to the large number of variables to optimize, it proved computationally inefficient. To address numerical limitations, an NSGA-II (Non-dominated Sorting Genetic Algorithm II) algorithm [28,55,56] was implemented from scratch in Mathematica© with the aim of obtaining the Pareto optimal sets and the Pareto frontier for several variables and objective functions. It is considered one of the most efficient methods among evolutionary methods for multi-objective optimization. A flowchart of all the required steps is presented in the paper by Li et al. [55], Fig. 4.

Very briefly, the first step is to generate a parent population. This is accomplished using a Monte Carlo sorting method. Specifically, 2.500 individuals are considered and sorted according to two criteria: rank (non-dominance) and crowding distance (the distance from an individual to its two closest neighbors). This ensemble is stored as an intermediate mating pool. In our case, these are 250 surviving individuals. Then, child populations are generated. This process includes crossover (simulated binary crossover) and mutation operators (polynomial mutation). It is necessary to verify that the new individuals belong to the physical region and satisfy its corresponding constraints. This is required because pseudo-random number generation could lead to unacceptable individuals. Subsequently, the parent population and their descendants are mixed and sorted with non-dominance and crowding criteria. Finally, the acceptable descendant population is stored.

The loop is then repeated until the Kullback–Leibler divergence or entropy (KLD) becomes small, meaning that more iterations will have a marginal impact on the search for new points. Details on the crowding distance, crossover, mutation and the convergence of the algorithm are included in Appendix B.

4. Validation and numerical implementation

In a previous publication [40], a detailed validation of all the subsystems conforming to the elected layout for the ACAES plant was presented. Thus, in this section, only a brief compilation is presented. For more details and graphical comparisons, refer to the cited publication.

4.1. Reference data and validation

The Huntorf plant (1978), located near Bremen in northern Germany, was the first commercial-scale CAES plant to come into operation [57]. Its original aim was to supply energy during periods of peak demand in an electric grid where nuclear power played a central role. Natural gas is burned to increase the temperature of the air at the outlet of the cavern before entering the expansion train. It has been taken as a reference for several research works on advanced CAES technology. It develops a power of about 200 MW with a maximum discharge time of 3 h and utilizes two salt caverns with a total volume of around 3×10^5 m^3.

With reference to the validation of the model for the air storage cavity, in Fig. 5, the simulated pressure and temperature for the air in a cavern with the same characteristics as those of Huntorf are presented. The methodology followed was explained in Section 3.1.2. Particularly, a discharge period of 16 h is presented. Differences between simulated and experimental results are small (the largest difference is for temperature, where difference reaches about 3°C). RMSE and MAPE errors are shown in Fig. 5. The reported increase in temperature at the end of discharge is achieved through the simulations; it results from the heat transfer from the cavern walls to the remaining air mass.

For condensing a brief validation of the evolution of the thermoclines of the PB systems in charge and discharge, Fig. 6 displays the evolution of the simulated thermoclines for a radial PB compared with the calculations from Trevisan et al. [46]. Charge and discharge are represented for the case of two layers with values of LR of 0.1 and 0.5 (see Section 3.1.3). In all cases, the dynamics of the temperatures inside the PB reservoirs are well attained. A more extensive validation of the model and the numerical methods used for simulating PBs dynamics can be found in [40,48].

For a validation of the whole system, integrating all the main components, the simulations from Sciacovelli et al. [58] were taken as reference. These authors consider an ACAES plant composed of a compression train with two compressors and intercooling between them, an axial packed-bed storage between the high-pressure compressor and the air cavern (see Fig. 1 in [58]). During discharge, the air exiting the cavern is heated in the PB before entering the expansion train, which consists of two turbines in series. Details on the dimensions of the cavern and other numerical data can be found in [40,58]. The most significant differences with our scheme, Fig. 1, are that in this paper, two PBs are considered, and they are radial for limiting pressure decays. Nevertheless, for validation purposes, the same scheme that was considered by Sciacovelli et al. was also simulated. Fig. 7 displays the evolution of three key variables for several charge-idle-discharge cycles (10 h charge, 10 h idle, and 4 h discharge): the thermal energy stored in the air cavern, the pressure inside, and the total power consumed by the compression train and produced in the expansion train during discharge. Figures show that differences are small. Also, a comparison of the PBs efficiency and the RTE of the whole plant is satisfactory (see Fig. 11 in [40]). For such a configuration, RTEs reached values around 0.75 (with both simulations, those by Sciacovelli et al. and the ones developed by our group) after stabilization during 20 cycles.

4.2. Multi-objective optimization: Decision variables and boundaries

In this subsection, the decision variables selected for optimization are described in detail. The allowed intervals and constraints for these variables are also outlined. The reference cavern volume is the aforementioned Huntorf plant ($V = 3{\times}10^5$ m^3). For the economic evaluation, in principle, an unbuilt salt cavern is taken as the initial case. The reference storage energy, $E_{c,stored}$, is 600 MWh. Considering a reference charging time, $t_{c,ref} = 3$ h, the charging power, $P_{c,ref}$, is 200 MW. The RTE of these kinds of plants is about 0.75 [40]. This means the energy released in discharge, $E_{d,stored}$, is about 450 MWh. This energy corresponds to a nominal power output, $P_{d,ref}$, of about 150 MW for an identical discharge time, $t_{c,ref}$, of 3 h. Huntorf's original plant has a considerably slower charging rate, resulting in lower charging power. In this work, a faster charging rate is considered. This strategy focuses on leveraging periods of low electricity prices to improve the plant's economic performance. The consequences will be discussed in the next sections. A quicker charge requires more power for the compressor train, which increases CAPEX. However, OPEX could be reduced by limiting charging to short periods when input energy prices are low.

4.2.1. Decision variables

Once the reference values for energy and power are selected, the next step is to choose which decision variables to optimize and the region over which they may vary. The most relevant variables for plant design are listed in Table 1. For clarity, note that the subindex ref

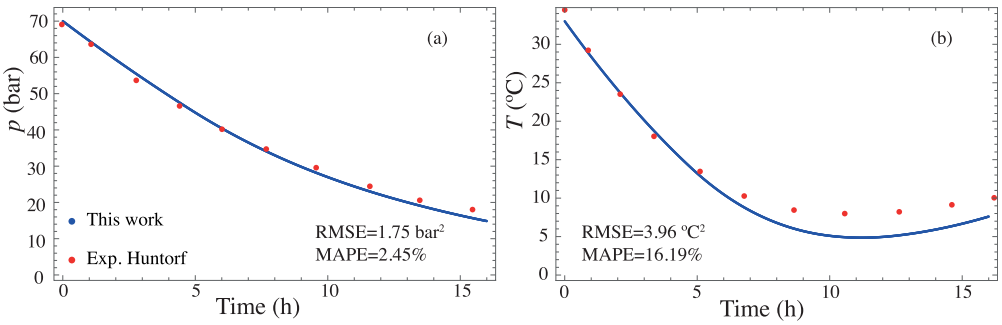

Fig. 5. Contrast between the experimental results from the Huntorf CAES plant [57] and the simulations in this work for the pressure (a) and the temperature (b) of the air in the cavern during a discharge process. The root mean square error (RMSE) and the mean absolute percentage error (MAPE) are shown for both variables as a guide to visualize the kindness of the simulations.

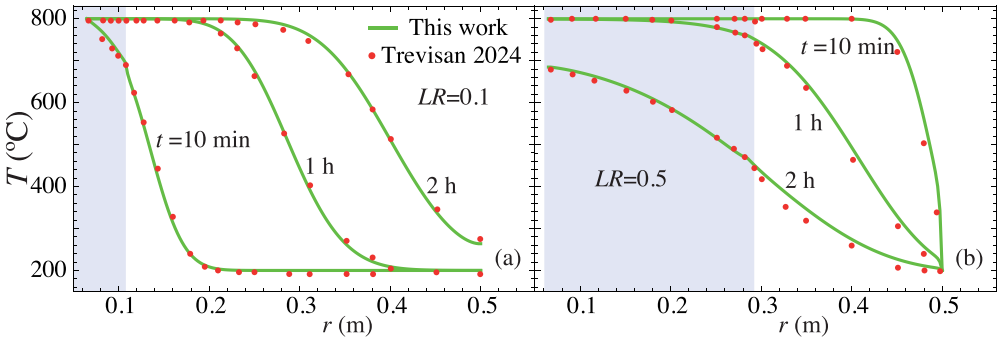

Fig. 6. Comparison of the thermoclines obtained for the radial PB with two coaxial layers in this work and the results from [46]. (a) Charge stage for $LR = 0.1$; and (b) discharge for $LR = 0.5$. The solid material is commercial ceramic Denstone© 2000.

Table 1
Intervals considered for the selected decision variables in the optimization process. Search range between 150–250 MW power and 2.25–3.75 h discharge time are taken.

Variable	Symbol	Min.	Max.	Unit
Nominal mass flow (charge)	$\dot{m}_{c,0}$	350	600	(kg/s)
Nominal mass flow (discharge)	$\dot{m}_{d,0}$	350	600	(kg/s)
TES dimensions	r_{out}-r_{in}	7	35	(m)
Internal TES radius	r_{in}	0	10	(m)
Layer ratio	LR	0	1	(–)
TES aspect ratio	AR	0.25	5	(–)
Initial cavern pressure	$p_{initial}$	30	90	(atm)
Maximum cavern pressure	p_{max}	40	75	(atm)
Minimum cavern pressure	p_{min}	55	90	(atm)
Pressure factor between compressors	δp_c	0.5	2.0	(–)
Pressure factor between turbines	δp_t	0.5	2.0	(–)

designates the reference Huntorf's plant, while the subindex 0 refers to the nominal value of each operation cycle. Variable values depend on time relative to their nominal values.

Nominal mass flow in charge, $\dot{m}_{c,0}$, is allowed to vary ±25% of the nominal reference value. $\dot{m}_{c,ref}$ can be obtained from the following equations:

$$E_{\mathrm{c,stored}} = P_{\mathrm{c,ref}} \cdot t_{\mathrm{c,ref}} = \dot{m}_{\mathrm{c,ref}} \cdot t_{\mathrm{c,ref}} \cdot \Delta h_{\mathrm{ref}}, \tag{16}$$

$$0.75\,\dot{m}_{\mathrm{c,ref}} \leq \dot{m}_{\mathrm{c/d,0}} \leq 1.25\,\dot{m}_{\mathrm{c,ref}}, \tag{17}$$

where Δh_{ref} refers to a reference specific enthalpy change in the compression train. It is an initial estimation calculated as the difference between the enthalpy at the exit of both compressors (h), and the enthalpy at ambient conditions (h_{amb}). Temperature and pressure at the exit are time-dependent, so for an initial estimation, the average charge magnitudes are used ($\bar{T}_{out}$, $\bar{p}_{out}$). Therefore, $\Delta h_{ref} = (h_{LPC}(\bar{T}_{out}, \bar{p}_{out}) - h_{amb}) + (h_{HPC}(\bar{T}_{out}, \bar{p}_{out}) - h_{amb})$. Thus, for charge, a reference mass flow of $\dot{m}_{\mathrm{c,ref}} = 475$ kg/s is obtained. The same criterion is followed for estimating the mass flow during discharge $\dot{m}_{d,0}$. In this case, $E_{\mathrm{d,stored}}$ cannot be calculated without solving system dynamics, so mass conservation is assumed and $t_{\mathrm{c,ref}}\dot{m}_{\mathrm{c,ref}} = t_{\mathrm{d,ref}}\dot{m}_{\mathrm{d,ref}}$.

The next variables to analyze are those associated with PBs dimensions. The radial length of the PBs is $r_{out} - r_{in}$. It is allowed to oscillate in a wide interval. Ideally, PBs should store a large amount of thermal energy, avoiding losses during thermocline degradation. LR values can range from 0 to 1, and the PB parameter, $AR = (r_{out} - r_{in})/H$, varies between 0.25 and 5. Constraints are detailed below.

Minimum and maximum pressures for the cavern are fixed between 40 and 90 atm. The minimum cavern pressure in the first cycle should be smaller than that in the subsequent cycles for a good pre-charge of the PBs. A parameter denoted δp_c is introduced for controlling the relationship between the pressure ratios of both compressors, LPC and HPC, at the end of the charge stage. Considering that:

$$p_{\mathrm{cavern}}/p_{\mathrm{amb}} = r_{p0,LPC} \cdot r_{p0,HPC}, \tag{18}$$

In symmetrical conditions, $r_{\mathrm{p0,LPC}} = r_{\mathrm{p0,HPC}} = \sqrt{p_{\mathrm{cavern}}/p_{\mathrm{amb}}}$ (which is simply the geometric mean between $r_{\mathrm{p0,LPC}}$ and $r_{\mathrm{p0,HPC}}$). In general, for non-symmetrical conditions, $r_{\mathrm{p0,LPC}} = \sqrt{p_{\mathrm{cavern}}/p_{\mathrm{amb}}} \cdot \delta p_c$ and $r_{\mathrm{p0,HPC}} = \sqrt{p_{\mathrm{cavern}}/p_{\mathrm{amb}}}/\delta p_c$. Thus, $\delta p_c = (r_{\mathrm{p0,LPC}}/r_{\mathrm{p0,HPC}})^{1/2}$.

For the expansion train, the procedure is similar.

$$p_{\mathrm{valve}}/p_{\mathrm{amb}} = r_{\mathrm{p0,HPT}} \cdot r_{\mathrm{p0,LPT}}. \tag{19}$$

For identical pressure ratios in both turbines, $r_{\mathrm{p0,HPT}} = r_{\mathrm{p0,LPT}} = \sqrt{p_{\mathrm{valve}}/p_{\mathrm{amb}}}$. And if they are different, $r_{\mathrm{p0,HPT}} = \sqrt{p_{\mathrm{valve}}/p_{\mathrm{amb}}}/\delta p_t$ and $r_{\mathrm{p0,LPT}} = \sqrt{p_{\mathrm{valve}}/p_{\mathrm{amb}}} \cdot \delta p_t$. Thus, $\delta p_t = \sqrt{r_{p0,LPT}/r_{p0,HPT}}$. Both parameters are allowed to take values between 0.5 and 2. This is a wide enough interval, aimed at avoiding physical inconsistencies.

Table 2
Physical restrictions for the decision variables.

Constraint	Variable of influence	Equation
(1)	Pressure	$15\,\text{atm} \le p_{\max} - p_{\min} \le 30\,\text{atm}$
(2)	Pressure	$40\,\text{atm} \le p_{\text{cavern}} \le 90\,\text{atm}$
(3)	Initial cavern pressure	$p_{\min} - 10.0 \le p_{\text{initial}} \le p_{\min}$
(4)	TES dimensions	$0.5\frac{E_{\text{thermal}}}{(1-\epsilon)\rho_s c_{p,s}\Delta T\eta_0\pi} \le \left(r_{out}^2 - r_{in}^2\right)\frac{r_{out}-r_{in}}{AR} \le 3.0\frac{E_{\text{thermal}}}{(1-\epsilon)\rho_s c_{p,s}\Delta T\eta_0\pi}$
(5)	Pressure drops (AR)	$r_{in} \ge 2.5\,\text{m};\quad 0.25 \le AR \le 2.5$
(6)	TIT	$\text{TIT}_0 - 120\ ^\circ\text{C} \le \text{TIT}(t) \le \text{TIT}_0$

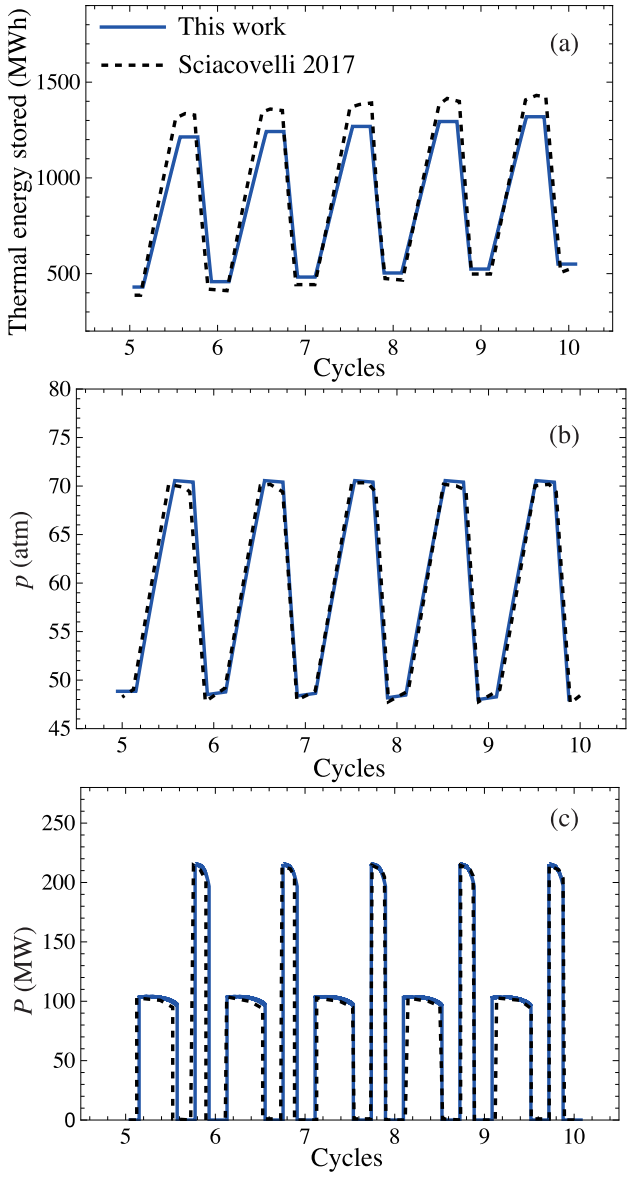

Fig. 7. Comparison of the results from the simulations developed in this work with those by Sciacovelli et al. [58] for several charge and discharge cycles. (a) Total thermal energy stored in the cavern; (b) pressure, p; and (c) power in the compression (with the sign changed for a better visualization) and expansion processes, P.

4.2.2. Constraints

Table 2 summarizes the constraints affecting the decision variables. They are numbered for an easier explanation.

- The first constraint (1) arises from the reference data for the energy stored in the cavern and the ideal gas law, because the stored energy is associated to the change of the pressure in the cavern during the charge process (supposed an approximately constant temperature): for $\dot{m}_{\text{c,ref}} = 475$ kg/s and $t_{\text{c,ref}} = 3$ h, $E_{\text{c,stored}} = 600$ MWh, it should be $p_{\max} - p_{\min} = (\dot{m}_{\text{c,ref}} t_{\text{c,ref}} RT)/(MV) \ge 15$ atm (M denotes the molecular weight of air). For the upper limit of the energy stored, it is considered $E_{\text{c,stored}} = 1300$ MWh, which is equivalent to $p_{\max} - p_{\min} = 30$ atm.
- Constraint (2) comes from the required conditions for the cavern itself. It should maintain a minimum pressure to avoid its collapse. This is especially important for salt cavities. On the other side, a maximum pressure has to be established. It depends on the depth of the cavern and the geophysical properties of the surrounding soil. As shown in Table 2, an interval from 40 to 90 atm is considered for the analysis in this work. This interval is for steady state conditions in cavern. However, pre-charge, *i.e.*, cycle number one, allows a lower pressure in the cavern, p_{initial}.
- Constraint (3) is arbitrary and it is assumed from the necessity to consider that during the pre-charge process, the minimum pressure is lower than in stationary operation. The established interval for the initial pressure is $p_{\min} - 10 \le p_{\text{initial}} \le p_{\min}$.
- Constraint (4) arises from the size of the PBs. Their dimensions can vary, but should be enough to store the energy from the air mass flow during the charge process (for instance, for the HP-PB). The total energy stored in the system can be expressed as the sum of the energy in the PBs (thermal) and in the cavern: $E_{\text{stored}} = 2E_{\text{thermal}} + E_{\text{cavern}}$ where $E_{\text{thermal}} = \dot{m}_{ref} t_{ref} c_{p,f} \Delta T$. This is the energy that the fluid entering, for example, HP-PB, contributes to the solid inside: the energy stored in the PB at the end of the charging process. For discharge, the reasoning is similar. In terms of the volume of each PB, V_{PB}, the void fraction, ϵ, the properties of the solid material on the PB, and an approximate efficiency value, η_0 (an approximate value $\eta_0 = 0.8$ is assumed), the energy stored in the solid can be expressed: $E_{\text{PB}} = (1-\epsilon)\rho_s c_{p,s}\eta_0 V_{\text{PB}}\Delta T$. For radial PBs, the volume can be written as: $V_{\text{PB}} = H\pi(r_{\text{out}}^2 - r_{\text{in}}^2)$ and $H = (r_{\text{out}} - r_{\text{in}})/AR$. Thus, substituting:

$$\left(r_{\text{out}}^2 - r_{\text{in}}^2\right)\frac{r_{\text{out}} - r_{\text{in}}}{AR} = \frac{E_{\text{thermal}}}{(1-\epsilon)\rho_s c_{p,s}\Delta T\eta_0\pi}. \tag{20}$$

In order to allow a wide variation on PBs dimensions, the following interval is considered:

$$0.5\,E_{\text{thermal}} \le E_{\text{PB}} \le 3.0\,E_{\text{thermal}}. \tag{21}$$

This interval can be rewritten as:

$$0.5\frac{E_{\text{thermal}}}{(1-\epsilon)\rho_s c_{p,s}\Delta T\eta_0\pi} \le \left(r_{\text{out}}^2 - r_{\text{in}}^2\right)\frac{r_{\text{out}} - r_{\text{in}}}{AR} \le 3.0\frac{E_{\text{thermal}}}{(1-\epsilon)\rho_s c_{p,s}\Delta T\eta_0\pi}. \tag{22}$$

This is a constraint on the size of the PB systems.
- Constraint (5) arises from restricting the pressure drops of the PBs. In a previous paper, it was demonstrated that, in a configuration similar to the one considered here, the pressure decay in the HP-PB is crucial; therefore, for optimization purposes, it should be limited. The limit is fixed at 1.5 atm; larger pressure decays are avoided. This implies certain conditions for the aspect ratio of the PB, AR, the internal diameter of the radial PB, r_{in}, and the

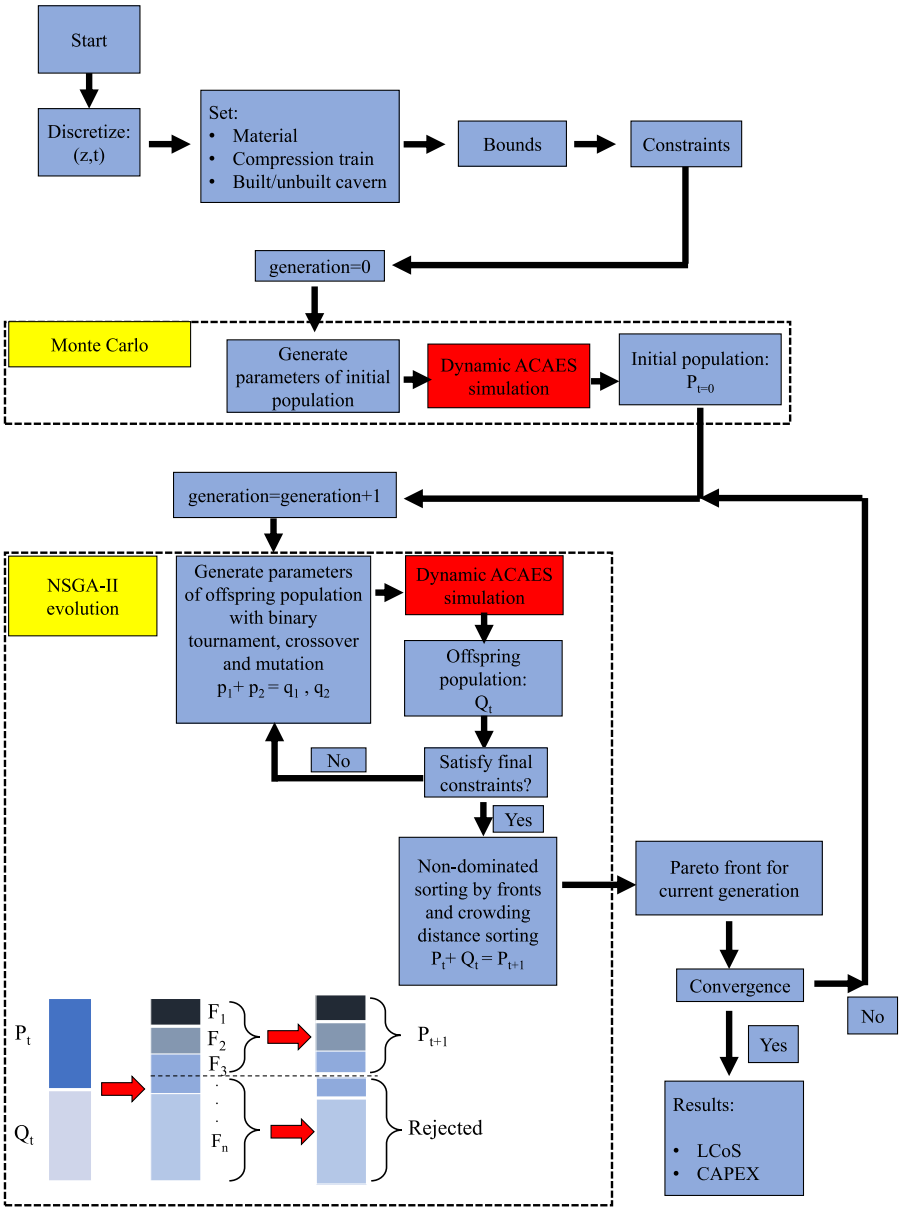

Fig. 8. Flow diagram of the optimization procedure.

Table 3
Constraints to be checked for each operation cycle.

Bond number	Variable of influence	Equation
(7)	Energy	450 MWh $\leq E_{out,1cycle}$
(8)	Pressure	15 atm $\leq p_{max} - p_{min}$
(9)	Temperature	$\Delta T_{bottom,TES} \leq 10$ °C

diameter of the particles, d_p. The constraint (5) in Table 2 comes from a previous numerical analysis on the pressure decays given by Ergun's formula, Eq. (8).

- Constraint (6) comes from the operation of the turbines during discharge. Their efficiency decreases significantly if the turbine inlet temperature (TIT), which depends on the time because the packed-bed temperature decreases, deviates from the nominal value, TIT_0. Differences below 120°C are not admitted.

Populations for optimization are generated by dynamically simulating plant behavior; therefore, some care must be taken to discard possible individual points that do not satisfy certain basic conditions. Table 3 summarizes this checking. Energy and pressure checks (7) and (8) are actually equivalent (total energy discharged in one cycle); however, a double check is performed to ensure accuracy. Initial charge pressure is p_{min}, final charge pressure is p_{max}, and final discharge pressure is also p_{min}. Condition (9) is important to avoid energy losses through the bottom of the PBs due to an underestimation of their dimensions or to an overestimation of the initial pre-charge pressure. Defining $\Delta T_{bottom,TES} = T_{bottom,TES} - T_{amb}$, this difference is limited to 10 °C.

For all simulated operation cycles, the idle time is fixed to two hours. This time is key for evaluating the LCoS. In the next sections, an analysis of this parameter will be done. Also, in all the results shown in Section 5, except explicitly mentioned, the price of electricity during the charge process is 50 €/MWh, that is an standard reference for comparing different storage technologies in Europe [33].

4.3. Simulations structure and implementation

The flow diagram in Fig. 8 displays the main steps of the optimization model's structure. The two main steps are highlighted in yellow.

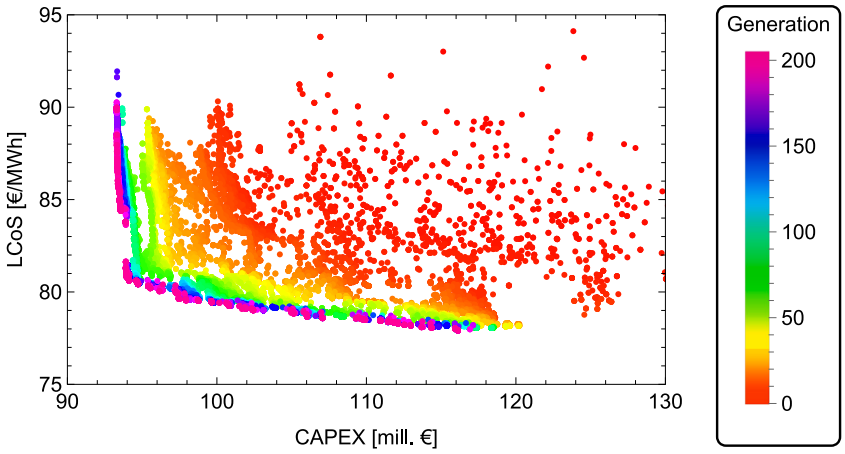

Fig. 9. Example of the evolution of generations through the NSGA-II algorithm until obtaining the Pareto front. The variables and their corresponding regions are presented in Table 1, and the constraints are those appearing in Table 2.

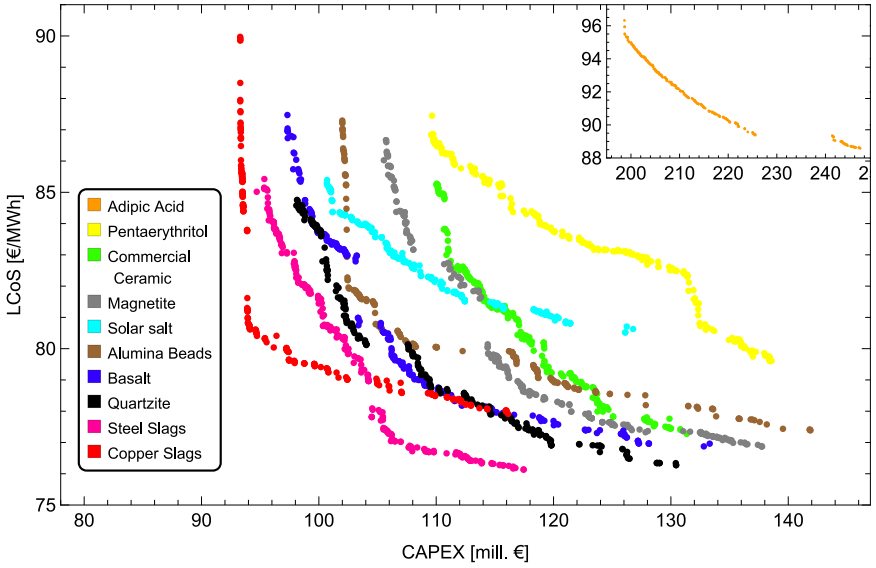

Fig. 10. Pareto fronts obtained for the analyzed materials, including sensible materials as well as phase-change ones: adipic acid, solar salt, and pentaerythritol (see text). Commercial ceramic corresponds to Denstone©2000 [59].

First, an initial population is generated using a Monte Carlo procedure. Next, new populations are generated according to the NSGA-II algorithm's conditions until the Pareto front is obtained. The red panels show the dynamical simulation of the ACAES plant. For each of these simulations, the flow diagram from Fig. 5 in [40] is used. In any generation, the dynamics of the plant subsystems (charge and discharge) are solved over several cycles until a stationary state is reached.

As an example of the evolution of the parent–offspring populations to non-dominated final conditions, Fig. 9 shows, using a color code, the representation of the objective functions LCoS and CAPEX. As mentioned in Section 3.3, the Kullback–Leibler divergence method is used to ensure stabilization of the Pareto front. It is observed that approximately 150 evolutionary generations are sufficient to reach convergence.

5. Results and discussion

In the next subsections, the Pareto fronts obtained from the optimization process are analyzed in detail.

5.1. Materials influence

Several materials have been analyzed for their potential as storage media, focusing on both sensible and PCM materials (see Fig. 10). For all simulations, a compression train with two centrifugal compressors is considered; the influence of compressor type is analyzed in the next subsection. Sensible materials evaluated include commercial ceramic (Denstone©2000) [59], copper slags, alumina beds, steel slags, basalt, magnetite, and quartzite (see Table A.9 in the appendix). These materials were selected based on availability, thermal properties, and cost considerations. For all of them, LCoS values are approximately 75–90 €/MWh, while the CAPEX has a wider interval. Copper slags are particularly notable due to their balance between high heat capacity ($\rho \cdot c_p$) and cost efficiency. Steel slags, which are potentially valuable as a metallurgical waste product, increase CAPEX but yield LCoS values similar to those of other materials.

For PCMs, it is essential to verify that their degradation temperature exceeds the maximum temperatures reached during charging and discharging. Latent materials analyzed are adipic acid [60,61] (solid–liquid), solar salt (liquid–solid, 60% $NaNO_3$ +40% KNO_3) [62–64], and

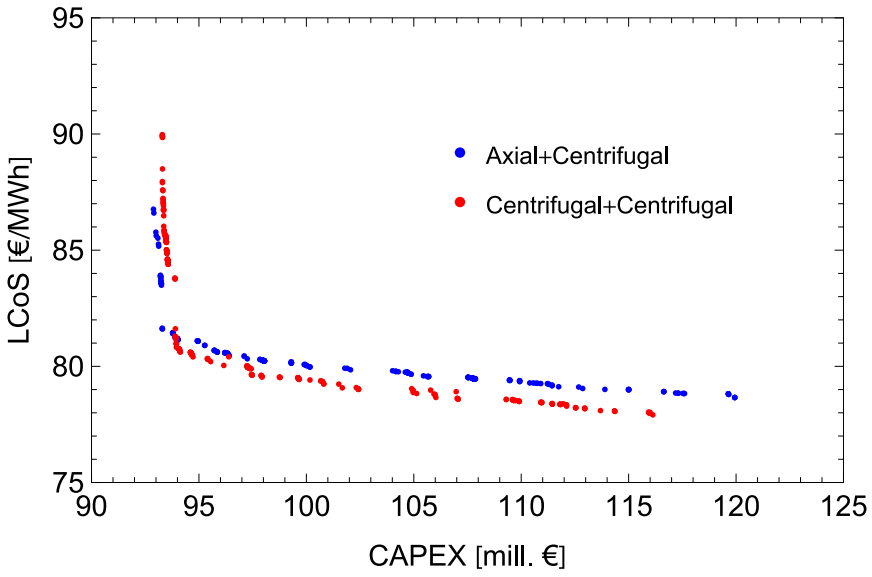

Fig. 11. Pareto front for two options on the compression train: low-pressure axial compressor and high-pressure centrifugal one (A+C, blue dots) and both centrifugal compressors (C+C, red dots).

pentaerythritol (solid–solid). For solar adipic acid and pentaerythritol [62], the Pareto fronts are shifted to the right and up. This indicates a worse thermo-economic performance for ACAES applications under the considered configurations (specially for adipic acid). Nevertheless, solar salt leads to not too high CAPEX values.

5.2. Compression and expansion trains analysis

From now on, copper slags in the packed-bed TESs are assumed for all the results presented. As discussed in Section 3.1.1, the most common configuration of compressors in CAES or ACAES plants with two-step compression is a low-pressure axial compressor with a fixed pressure ratio. The second stage is a high-pressure centrifugal compressor that works at a variable pressure ratio during the charge process (option A+C). A less common combination uses two centrifugal compressors operating along their best efficiency lines (option C+C). From a thermodynamic viewpoint, as reflected in the round-trip efficiency, the second option also appears reasonable, as shown in [40]. Therefore, this study analyzes the economic differences between the two options.

Fig. 11 shows the Pareto fronts obtained using LCoS and CAPEX as KPIs. Both Pareto fronts overlap, indicating that neither option is clearly superior across all KPI intervals. Option A+C (blue points in the figure) leads to a narrower LCoS interval (approximately between 79 and 87 €/MWh). In contrast, option C+C provides a wider interval for possible optimal LCoS values (approximately 78–90 €/MWh). Optimal values for CAPEX behave opposite: the configuration A+C leads to a wider interval (93–120 mill. €) than C+C (94–116 mill. €).

One way to visualize the relationship between the round-trip efficiencies and the optimized KPIs for the two options considered in the compression train is to assign a color code to points on the Pareto fronts based on the corresponding RTE. This is displayed in Fig. 12. The panel at the left corresponds to the option centrifugal + centrifugal (C+C). In this case, there is a wide range of RTEs at the front points, from about 0.70 to 0.79. The other option, A+C, leads to a interval for the corresponding RTEs between approximately 0.70 and 0.78. The crosses in the panels indicate the points with the higher RTE values. This result is in accordance with the previous estimations of RTEs for both options in [40]. Thus, the configuration C+C is selected from now on due to its high RTE and its greater dominance on the Pareto front compared to A+C.

The parameter δp_c was defined in Section 4.2 to consider the symmetry ($\delta p_c = 1$) or lack of symmetry ($\delta p_c \neq 1$) of the pressure ratios of the centrifugal compressors: $\delta p_c = (r_{p0,LPC}/r_{p0,HPC})^{1/2}$. As it is seen in Fig. 13(a), the points of the Pareto front have values for δp_c between 0.55 and 1.1 approximately. For simplicity, $\delta p_c = 1.1$ would correspond to a pressure ratio of the HPC (at the end of the charge process) lower than that of the LPC, about 0.82 times lower, and at the other extreme, $\delta p_c = 0.55$ would be associated with a pressure ratio of the HPC 3.3 times larger than that of the LPC. The lowest CAPEX values correspond to the symmetric case, and the highest to δp_c between 0.6 and 0.7, that is, an HPC with a pressure ratio three times that of the LPC. The lowest LCoS values are found in the latter case. As observed in the figure, low δp_c values are more frequent because they reduce the maximum pressure of the PB-LP and, thus, its mechanical isolation from pressure stresses and costs.

An analogous analysis is done for the turbines in Fig. 13(b). For the expansion train, pressure ratios are referred to the pressure at the throttling valve: $\delta p_t = (r_{p0,LPT}/r_{p0,HPT})^{1/2}$. In this case, the points of the Pareto front always correspond to values of $\delta p_t < 1$. This indicates that the HPT pressure ratio is larger than that of the LPT. The smallest values of LCoS correspond to δp_t between 0.6 and 0.7. For these points, the pressure ratio of the HPT is between 2.0 and 2.8 times that of the LPT. This tendency in the turbines ($r_{p0,HPT} > r_{p0,LPT}$) likely originates from the similar behavior of the compressors. In compressors, $r_{p0,HPC} > r_{p0,LPC}$. This is likely because the packed-beds charge and discharge at equivalent pressures, making a more efficient use of the stored energy.

5.3. Analysis of Pareto fronts and decision variables

In this subsection, the Pareto fronts of LCoS vs CAPEX are presented for radial packed-beds with copper slags inside, option C+C for the compression train, and an unbuilt salt cavern. The objective is to analyze some supporting performance indicators related to energetic variables, charge and discharge times, cavern pressures, packed-bed geometrical dimensions, and others.

5.3.1. Energetic indicators

Fig. 14 displays the points of the Pareto fronts classified in terms of several energetic indicators. These include input and output energies and powers. For example, the first row of panels in the figure shows the composition of the points in terms of specific CAPEX (or energy/power capital costs). This is given either per unit output energy in one cycle, as in Fig. 14(a), or per unit power output, as in Fig. 14(b). Energy-specific CAPEX (€/kWh) changes from approximately 240 (high LCoS

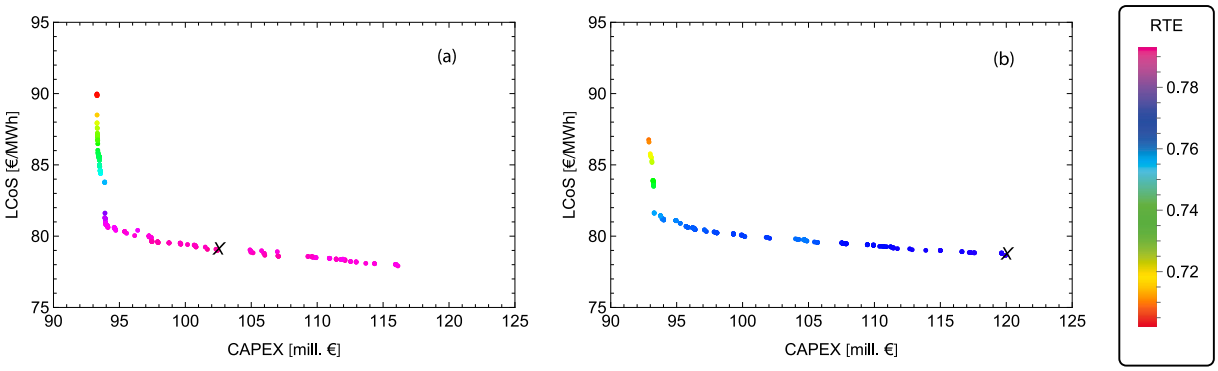

Fig. 12. Pareto fronts for the considered compression trains displaying the RTE in each case: (a) option C+C and (b) option (A+C). The crosses indicate the points with a higher RTE.

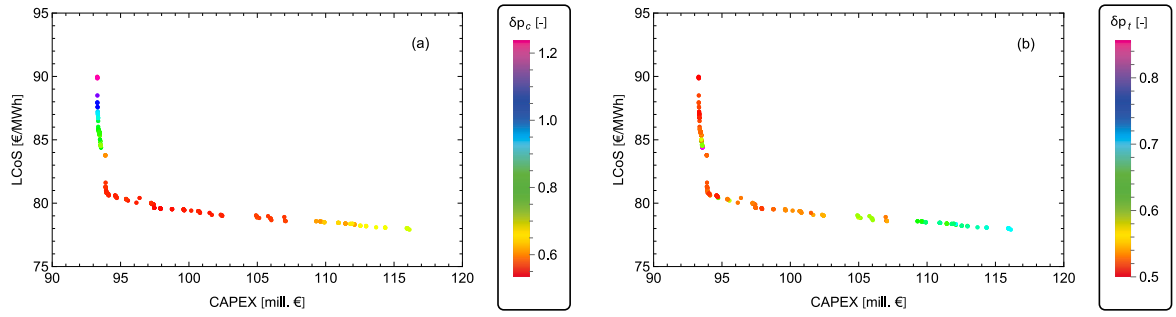

Fig. 13. Sensitivity of the Pareto front to the ratio between the pressure ratios of (a) compressors, δp_c, and (b) turbines, δp_t. The configuration C+C is considered for the compression train.

and low CAPEX) to 140 (low LCoS and high CAPEX). These values are in agreement with those estimated by Mersch et al. [32]. Power-specific CAPEX is in the interval 600–750 €/kW. In both figures, the evolution is similar; specific CAPEX decreases to the bottom and the right (lower LCoS, higher CAPEX and RTE). The crosses in the panels of the figure indicate the minimum value of specific CAPEX.

The mid and bottom panels of Fig. 14 display the evolution of the optimum configurations with input and output energies, Figs. 14(c) and (d), and with input and output powers, Figs. 14(e) and (f). In all cases, the evolution is similar: as LCoS decreases and CAPEX increases, energies and powers increase. Input energies range from 500 to 1000 MWh, and output energies range from approximately 400 to 800 MWh. Input powers range from 160 to 260 MW, corresponding to outputs from 125 to 195 MW.

5.3.2. Charge/discharge times and mass flows

Figs. 15(a) and (b) shows the charge, t_c, and discharge times, t_d, of the optimum configurations of the Pareto front in the considered ranges. Idle time is fixed to two hours always. In this case, there is no simple linear evolution of colors in the figures; actually, there are leaps showing that different combinations of t_c and t_d within those intervals (between 3 and 4.25 h for both stages) can lead to optimum values of LCoS and CAPEX.

The points of the Pareto front (the set of optimal solutions balancing competing objectives) are analyzed in terms of the charge and discharge mass flows in Figs. 15(c) and (d). For the charge phase, all the considered intervals for $\dot{m}_c$ (the mass flow rate during charging) are approximately 350–500 kg/s. Lower CAPEX and higher LCoS are achieved with lower mass flow, and conversely. Nevertheless, for discharge, the covered mass flows, $\dot{m}_d$ (the mass flow rate during discharging), are within a narrower interval, from 350 to 440 kg/s. This is because axial turbines are more expensive for higher mass flows, so the optimization results in the smallest flows.

5.3.3. Pressures in the high-pressure reservoir

The role played by the pressures of the air inside the cavern is investigated through the plots in Fig. 16. The allowed intervals for pressures and the corresponding constraints are those established in Section 4.2. The Pareto front evolves similarly with the initial pressure (p_{ini}), as well as the minimum and maximum values (p_{min} and p_{max}). Lower LCoS values are obtained for high pressures. Conversely, larger values are found for lower pressures. CAPEX changes in the opposite way. High CAPEX is associated with high pressure values. Optimum pressure values are spread throughout the considered intervals, which are shown in the color code panels. Conversely, the pressure gradient in the cavern (Δp_{cavern}, Fig. 16(d)) takes values in the bottom region. The lowest CAPEX is observed for values around 16–18 atm, while the lowest LCoS is found for values around 26 atm.

5.3.4. Packed-bed geometry

Some geometrical parameters of the two radial packed-beds, considered identical, are analyzed in Fig. 17. The intervals considered for those parameters and the related constraints are detailed in Sec . 4.2. The height of the packed-bed containers, H (Fig. 17(a)), decreases in the Pareto front from the top left to the bottom right. The largest LCoS is expected at the largest H values, around 8 m for the considered configuration and numerical parameters. Oppositely, the lowest ones are found for H about 6 m. The internal TES radius, r_{in}, admits different values to get lower values of LCoS (leaps on the Pareto front shown in Fig. 17(b)). The range of its values is 2.5–4.5 m. The thickness of the two layers of solid, $r_{out} - r_{in}$ (Fig. 17(c)), is more probable in the lower zone of the searched interval, between 10 and 12 m. Finally, the layer ratio, $LR = (r_{layer} - r_{in})/(r_{out} - r_{in})$ (Fig. 17(d)), has small values (between 0.025 and 0.15), indicating that the thickness of the outer layer is considerably larger than that of the internal one in the optimum configurations of the Pareto front. Some jumps are also observed in the figure, indicating different options for selecting LR.

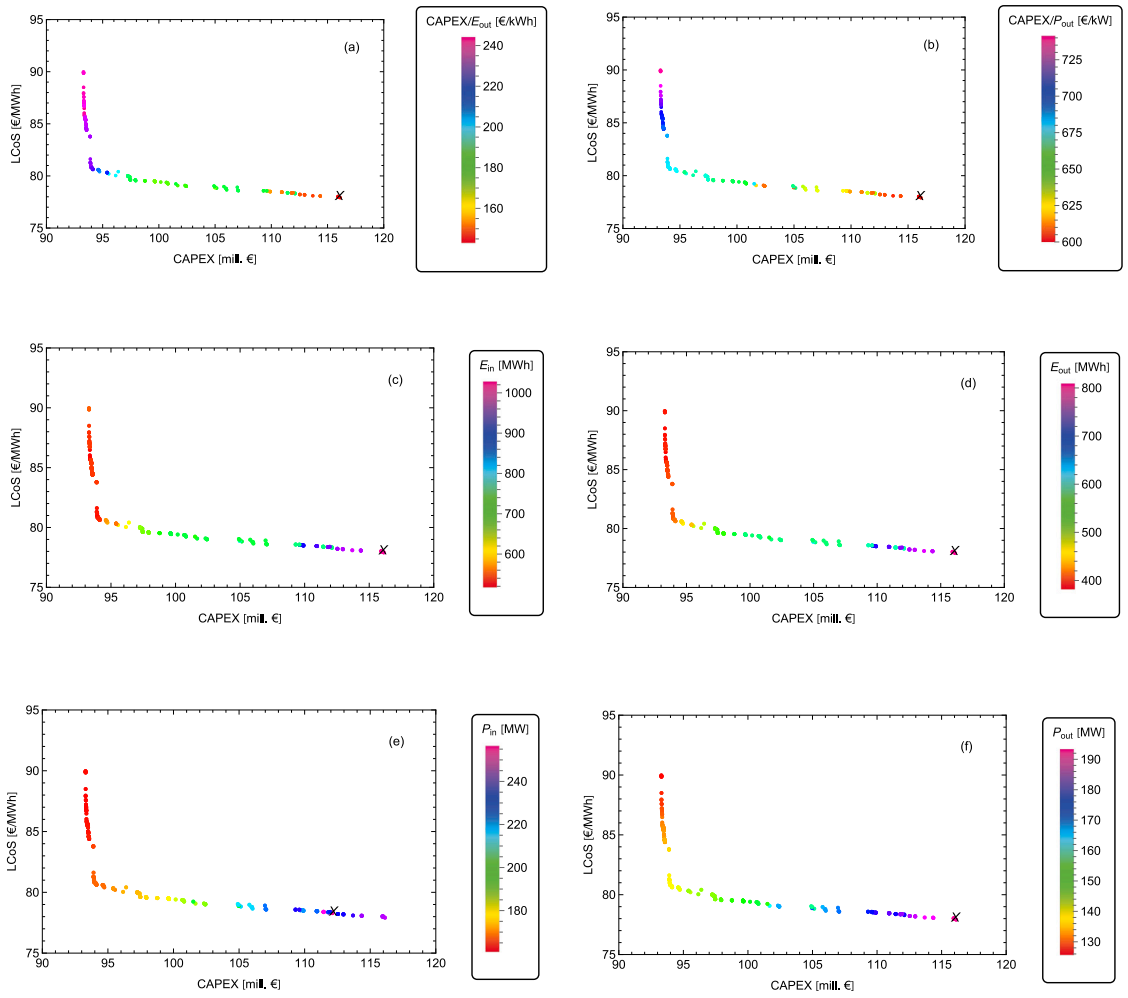

Fig. 14. LCoS vs CAPEX Pareto fronts with code color for different energetic indicators: (a) Energy-specific CAPEX; (b) Output power-specific CAPEX; (c) Input energy in charge; (d) Output energy in discharge; (e) Power consumed for charge; and (f) Power output during discharge. The crosses indicate always the point with maximum or minimum value of the analyzed parameter.

5.4. Influence of the cavern type

A fundamental element in construction costs is the high-pressure air reservoir or cavern. In this section, two salt cavern options are surveyed (see Fig. 18): a preexisting (built) one (for instance, an abandoned natural gas well) or a cavern specifically constructed (unbuilt) for the plant (for instance, injecting water to form a cavern in a rock mantle or salt deposit). Data and correlations for both cases are detailed in the Appendix, Table A.8. As the figure illustrates, the values of LCoS and CAPEX depend significantly on this element. For unbuilt caverns, the largest LCoS reaches values about 90 €/MWh. This is reduced to 85 €/MWh for a preexisting cavern. With respect to CAPEX, a plant with all the considered parameters (configuration, size, energy, and power levels, etc.) and an unbuilt cavern requires at most 115 million €. And this is reduced to roughly 75 million € with a preexisting reservoir. The option of lined-rock caverns was also surveyed (see data in the appendix, Table A.7), but it is disregarded because CAPEX results are much higher.

5.5. Sensitivity to the electricity price during charge and the idle time

Up to this point, all the LCoS values shown in the Pareto fronts have been obtained assuming a reference electricity price of 50 €/MWh during the charge phase. To clarify the impact of electricity prices on LCoS, this subsection examines their influence on final LCoS values. Fig. 19 presents this sensitivity for an unbuilt cavern. As shown, LCoS values decrease with lower electricity prices, reaching below 20 €/MWh in the extreme (limit) case of free electricity. Conversely, higher purchase prices, such as 100 €/MWh, result in LCoS values of around 140 €/MW. These results suggest that ACAES systems perform especially well economically during periods of abundant renewable energy. Further details, including interpolation functions for the expected Pareto front curves of LCoS vs CAPEX, are provided in Appendix A.4.

With the aim of examining the significance of the LCoS values obtained for the considered ACAES type of plant, an analysis of the sensitivity of LCoS to idle time has been performed. Idle time does not affect the dynamics of charge or discharge, but it determines the total number of cycles per year and, thus, affects the LCoS. Larger idle time leads to more inactivity periods in the plant and larger LCoS values. This is clear from Eqs. (14) and (15). The dependence of LCoS with the idle time is presented in Fig. 20 where the reference plant size data exposed in Section 4 were assumed (centrifugal compressors, copper slags in the packed-beds, a price of electricity of 50 €/MWh, and an unbuilt air deposit). In particular, the idle reference time reported here (and in all previous results) was 2 h. This election corresponds to a plant used for peak shaving. Another option is to consider larger times for load shifting. This is why larger times are analyzed. As shown in the figure, LCoS increases linearly with the idle time. Minimum

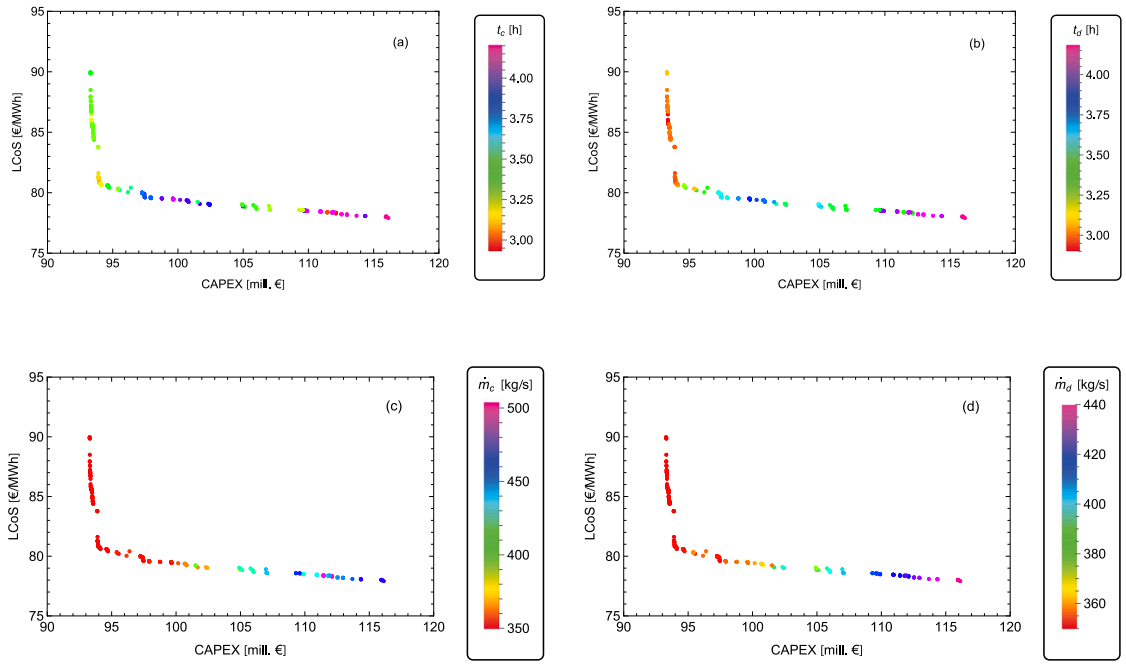

Fig. 15. Influence of (a) charge time, t_c; (b) discharge, t_d; (c) charge mass flow, $\dot{m}_c$; and (d) discharge mass flow, $\dot{m}_d$, on the optimum configurations.

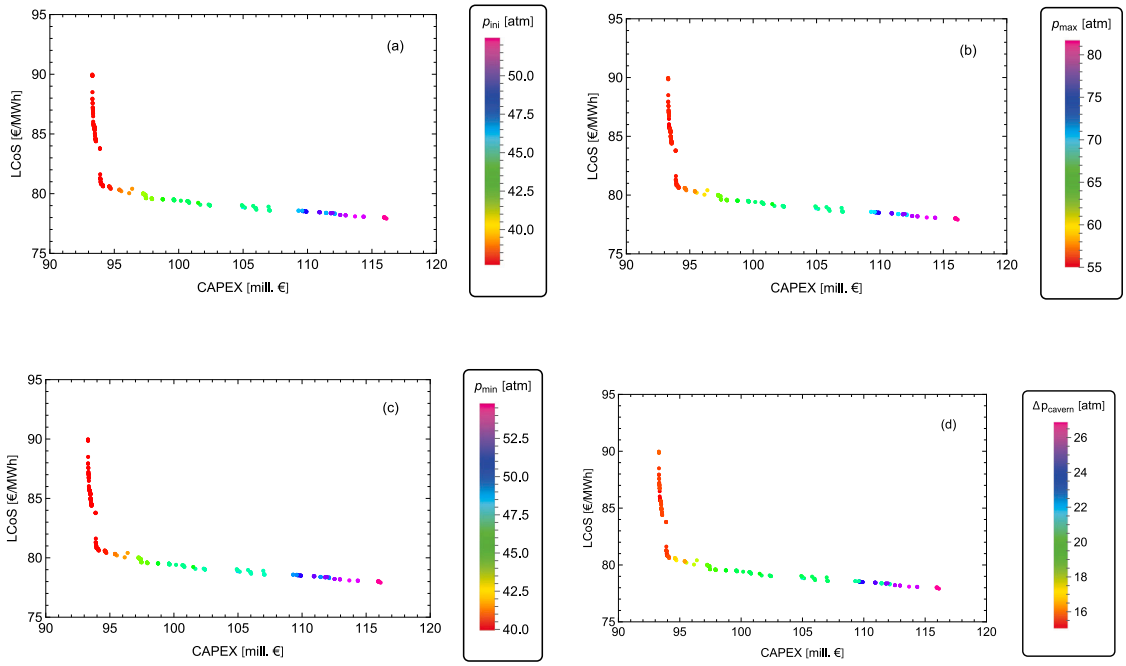

Fig. 16. Influence of the initial pressure in the cavern: (a) the initial pressure in the cavern, p_{ini}, the maximum and minimum pressures, p_{max} (b) and p_{min} (c), and (d) the difference between them, Δp_{cavern}.

LCoS values for short storage periods are slightly below 80 €/MWh, but as idle time increases, LCoS rises. Just to have a reference, for idle times around 24 h (load shifting), LCoS is predicted to amount to about 100 €/MWh, and for 48 h (it is important to remark here that packed-beds are capable of storing energy for periods of about 40 h without significant efficiency decrease), roughly 130 €/MWh. This analysis should be considered preliminary; it is an open field for future studies based on the methodology developed in this work. A more thorough analysis should include the variability of electricity prices across regions and possible operational strategies for charging, discharging, and idle times.

5.6. Subsystems CAPEX and costs example

Fig. 21 and Table 4 contain illustrative data for a particular ACAES plant configuration. The results correspond to a point of the Pareto front displayed in Fig. 14, particularly to the point giving the minimum specific CAPEX relative to the output energy, CAPEX/E_{out} (see the cross marked in Fig. 14(a)). Several considerations should be taken into account before analyzing the results. Cost correlations for turbomachinery are quite dissimilar in the literature (see tables in the Appendix). Costs for compressors are taken for centrifugal ones: for instance, the considered centrifugal LPC amounts to 13.21 mill. € and a comparable

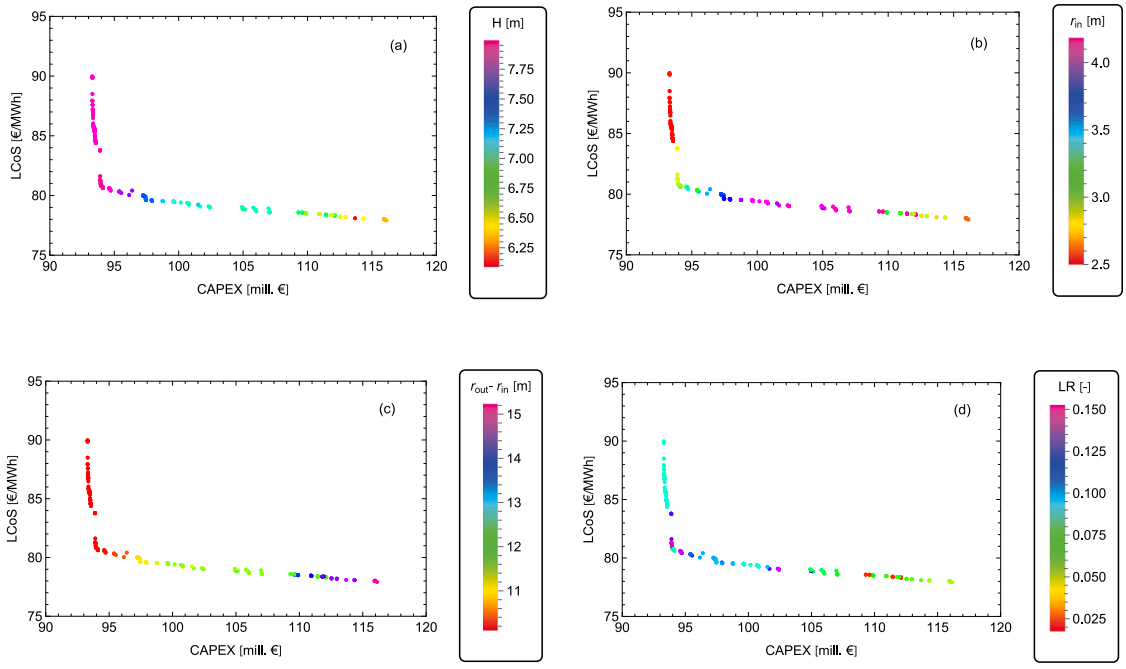

Fig. 17. Influence of some geometrical parameters of the radial packed-beds (see Fig. 4): (a) H, height; (b) r_{in}, radius of the internal tube; (c) $r_{out} - r_{in}$; and (d) LR, layers ratio.

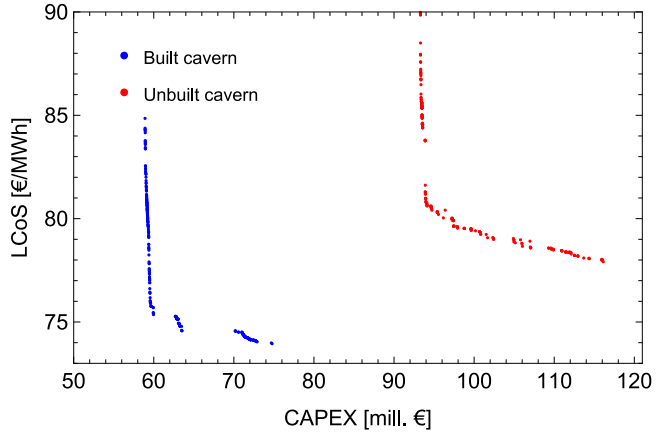

Fig. 18. Pareto fronts built with costs correlations associated to a preexistent salt cavern (built) or one specifically built for the ACAES plant (unbuilt).

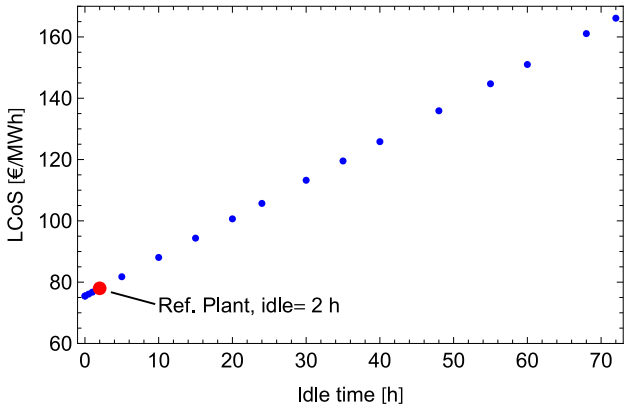

Fig. 20. Sensitivity of the LCoS to the idle time. The linear fitting leads to this correlation: LCoS [€/MWh]= 75.4731 +1.25901 × Idle time [hours].

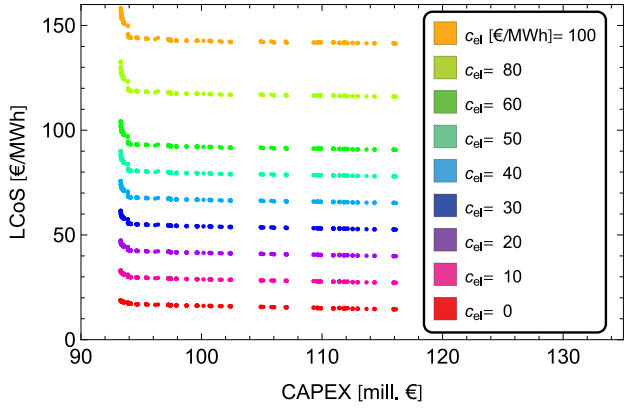

Fig. 19. Sensitivity of the Pareto fronts to the prices of electricity during the charge stage, C_{el} in the case of an unbuilt cavern.

axial one about 7.8 mill. €, so different CAPEX would be obtained. However, as explained earlier, this work considers a configuration with two centrifugal compressors. Regarding turbine prices, it is essential to note that they depend significantly on the TIT. In this case, a combustion chamber is not required, and the temperatures reached are not very high, so the price is reduced.

For an idle time of 2 h, an unbuilt cavern, and copper slags for the TES materials, the total CAPEX (see Table 4) amounts to about 116.54 mill € and the OPEX for one-year operation considered, 45.75 mill€. This leads to an LCoS of about 78 €/MWh (with a purchase price of electricity of 50 €/MWh). As shown in Fig. 21, the cost of the cavern is about 28% of the total CAPEX. The compression and expansion trains account for about 34.3% of the total CAPEX, and the thermal storage for about 9.5%. These percentages are very close to those estimated by Tian et al. [27] for an ACAES plant of 300 MW (see Table 5 therein). The main difference is that they estimate a lower percentage for the air storage, 14.5% (for a 4.58×10^5 m^3 volume).

Table 4
Costs of plant components corresponding to the configuration giving the minimum value of CAPEX/E_{out} (cross marked in Fig. 14(a), see text for other details). The annual OPEX is also shown. Annual energy yield (AEY) is 676.76 GWh. The column on the right shows the percentage cost of the main plant subsystems in the total CAPEX.

Item	Value (mill.€)	Percentage over CAPEX (%)
LPC	13.21	
HPC	18.06	
HPT	5.15	Turbomachinery
LPT	3.54	34.29
High-pressure air storage	32.51	27.90
LP-PB	1.68	Thermal storage
HP-PB	9.35	9.46
Generator	1.62	
Heat exchanger	0.035	
Land+site	0.022	Land and other hardware
Piping	3.0	4.00
BOP	8.62	Other (financial)
Contingency+EPC	19.76	24.35
CAPEX	116.54	100.0
O&M fix (one year)	1.90	
O&M var(one year)	0.90	
Cost of electricity charge in one year	42.95	
OPEX (one year)	45.75	
LCoS	77.99 €/MWh	

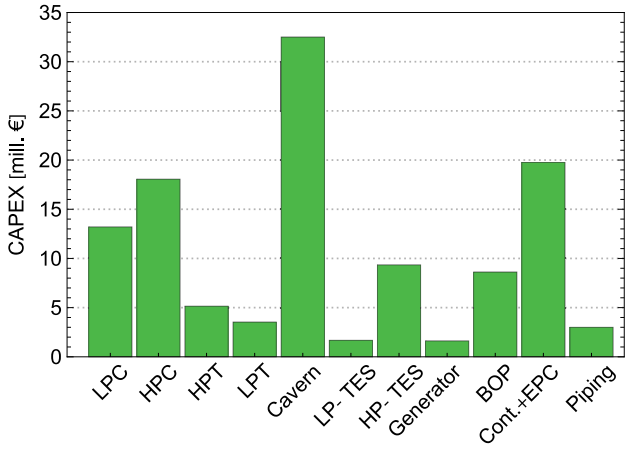

Fig. 21. Costs of plant components included in the CAPEX. Data correspond to the configuration giving the minimum value of CAPEX/E_{out} (see the cross marked in Fig. 14(a)).

6. Summary and main conclusions

As discussed in the Introduction, most thermo- or techno-economic analyses of ACAES systems in the literature rely on models that make coarse assumptions. These models are not fully dynamic across all components. As a result, there is a wide range in the expected economic indicators for this technology, such as LCoS. The global objective of this work was to develop a sensitivity and optimization analysis based on a detailed, realistic, and fully dynamic model for an ACAES plant configuration. This configuration a priori has satisfactory thermodynamic performance, as shown in previous studies [40].

This plant configuration features a compression train consisting of two centrifugal compressors in series or a mixed axial/centrifugal arrangement. Two packed-bed thermal energy storage systems store thermal energy from the compressors' outlets during the charge phase. They are designed radially to minimize pressure losses and can contain either sensible or phase-change materials. During the charge step, compressed air is stored in a reservoir, which can be an existing geological formation, such as a salt cavern, or a reservoir prepared specifically for the plant. The models for packed-beds and the air reservoir are dynamic, so it is possible to track the evolution of both subsystems over time and obtain precise values of the round-trip efficiency. In the discharge phase, the air at the exit of the reservoir is heated by the high-pressure packed-bed and then passes through a throttling valve that approximately maintains the inlet pressure of the expansion train. The latter consists of two axial turbines in series. Between them, the working fluid is heated in the low-pressure packed-bed. A heat exchanger is installed at the outlet of the first turbine to prevent thermocline degradation in the low-pressure packed-bed. All plant subsystems and the overall system were validated against previous works. The well-known Huntorf plant was considered for sizing a reference plant.

The key performance indicators selected for the optimization process are the levelized cost of storage and the capital expenditure. To obtain the Pareto-optimal sets and the Pareto frontier, an adapted genetic algorithm was used. Several physical parameters were taken as decision variables; specifically, times and mass flows in charge and discharge, PB dimensions and layer ratio, and the minimum and maximum pressures in the cavern were allowed to vary within reasonable intervals. To ensure robustness, possible restrictions among variables were carefully analyzed, along with the economic correlations and data used in the calculations.

The values obtained for LCoS on the Pareto front for a base case with two centrifugal compressors, copper slags in the packed-beds, a reference stored energy of 600 MWh, an idle time of two hours, an unbuilt cavern, and a reference price for electricity of 50 €/MWh, are in the interval 75–90 MWh. This interval lies in the lower range of LCoS estimations reported in the literature (see Introduction). CAPEX interval in such conditions is between 94 and 120 mill.€ approximately. Other significant conclusions of the work can be summarized as follows:

- The selection of the material for the PBs is more influential on CAPEX than on LCoS. Sensible materials, specifically copper slags, lead to the Pareto fronts with lower CAPEX values. Steel slags, that may be interesting as a waste from the metallurgical industry,

also may be interesting. Several PCMs were also checked and, except for solar salt (which does not greatly increase LCoS or CAPEX), led to higher CAPEX.
- The configuration of the compression train is important. The C+C configuration (two centrifugal compressors) achieves better LCoS values but at a higher CAPEX than the A+C configuration (low-pressure axial and high-pressure centrifugal compressors). Values of RTEs in the scheme C+C are around 0.76–0.78 for the points in the Pareto front. These efficiencies are in concordance with other studies on ACAES systems.
- Energy-specific CAPEX (€/kWh) is in the interval 140–240, and power-specific CAPEX (€/kW) is in the interval 600–750. Despite the fact that each considered configuration has design peculiarities, these values are consistent with the results of several previous works [25,27,36,37,39].
- Charge and discharge times leading to optimum values of LCoS and CAPEX are in the interval 3–4.25 h, with a fixed idle time of 2 h.
- With respect to the pressures in the air reservoir, they lead to optimal values of LCoS and CAPEX when the maximum is between 55 and 85 atm, the minimum between 40 and 55, with a difference of about 16–26 atm.
- A significant difference in the values of LCoS and CAPEX was found when comparing an unbuilt geologic air reservoir with a built one (for instance, an existing salt cavern). While for the first LCoS varies between 72 and 85 €/MWh (CAPEX between 60 and 75 mill.€), in the second it varies between 78 and 90 €/MWh (CAPEX between 92 and 115 mill.€).
- The sensitivity of LCoS values to the electricity price during the charge period was also analyzed, with a reference price of 50 €/MWh. High prices (for instance, about 80 €/MWh) can push LCoS to around 120 €/MWh. On the other hand, at very low electricity prices, LCoS can decrease to 20–40 €/MWh. Specific correlations are provided in Appendix. These results reinforce the idea that ACAES systems can be highly compelling for storing electricity from renewable PV or wind installations during high production periods.
- The behavior of LCoS with the idle time is almost linear.
- Relative costs of subsystems in plant CAPEX have also been estimated. The largest weight is for the compression and expansion trains (about 35%). If the cavern is considered unbuilt, the compression train's costs can reach those of the air reservoir (about 28%). The cost of turbines is smaller because they do not operate at very high temperatures. There is a significant difference in the costs of the thermal energy storage units: the high-pressure packed-bed subsystem costs at least 4 times as much as the low-pressure one (both cost about 9.5% of total CAPEX). The proportion of subsystems in the CAPEX is also consistent with previous analyses of similar ACAES configurations [27].

In brief, this work provides detailed and precise design guidelines for the promising ACAES technology in the context of indispensable large-scale, reliable, and economically affordable energy storage systems for sustainable energy production. A key future investigation to assess the possible strength of this technology relative to other alternatives is an environmental impact study, for instance, using a life-cycle analysis (LCA) methodology.

CRediT authorship contribution statement

D. Pérez-Gallego: Writing – review & editing, Writing – original draft, Validation, Software, Methodology, Investigation, Conceptualization. **J. Gonzalez-Ayala:** Writing – review & editing, Writing – original draft, Supervision, Software, Methodology, Investigation, Conceptualization. **A. Medina:** Writing – review & editing, Writing – original draft, Visualization, Supervision, Investigation, Funding acquisition, Conceptualization. **S. Anvari:** Writing – review & editing. **I. Calderón-Vásquez:** Writing – review & editing. **J.M. Cardemil:** Writing – review & editing. **A. Calvo Hernández:** Writing – review & editing, Writing – original draft, Supervision, Project administration, Investigation, Conceptualization.

Declaration of competing interest

The authors declare the following financial interests/personal relationships which may be considered as potential competing interests: David Perez-Gallego reports financial support was provided by Junta de Castilla y León Consejería de Educación. Alejandro Medina reports financial support was provided by Spain Ministry of Science and Innovation. David Perez-Gallego reports a relationship with Junta de Castilla y León Consejería de Educación that includes: funding grants. If there are other authors, they declare that they have no known competing financial interests or personal relationships that could have appeared to influence the work reported in this paper.

Acknowledgments

D. Pérez-Gallego thanks financial support from Fondo Social Europeo Plus and Consejería de Educación de la Junta de Castilla *y* León under their Ph.D. grant program (EDU/1868/2022). S. Anvari thanks a fellowship within the Energy for Future (E4F 2024/25) program funded by Fundación Iberdrola España and Universidad de Salamanca. Funds from Ministerio de Ciencia, Innovación *y* Universidades of Spain under grants PID2023-147201OB-I00 and RED2024-153629-T; from Consejería de Educación de la Junta de Castilla *y* León under grant SA071G24, and from Universidad de Salamanca are also acknowledged. The authors acknowledge Judit García-Ferrero for her support in modeling the compression and expansion trains.

Appendix A. Thermo-economic data and correlations

A.1. Correlations for CAPEX calculations and costs

Table A.5 displays the correlations used to estimate plant's CAPEX. For axial compressors, f_c is defined as:

$$f_c = 1/(\eta_{ref,c} - \eta_{poly}). \tag{23}$$

For axial turbines, $f_{\mathrm{T,turb}}$ and f_t, are defined as:

$$f_{\mathrm{T,turb}} = 1 + e^{0.025\cdot(\mathrm{TIT[K]}-1600)}; \quad f_t = 1/(\eta_{ref,t} - \eta_{poly}). \tag{24}$$

The calculation of costs correlations of the thermal energy storages follows the procedure by Seider et al. [53]. $f_{\mathrm{T,TES}}$ is always equal to 1 in this plant because temperatures are not too high ($T < 560$°C).

In Table A.6, all the reference parameters for costs are shown.

A.2. Air reservoir costs

Tables A.7 and A.8 contains the cost considered for the air reservoir, either lined-rock cavern or salt cavern.

A.3. Packed-bed materials properties

Table A.9 presents key physical properties and prices of the evaluated materials. Some of them are sensible heat storage materials, which store energy through a temperature change, while solar salt, adipic acid, and pentaerythritol are phase-change materials (PCM) that store energy through a phase-change. Although adipic acid is more expensive, its higher energy density can reduce the size of the PBs and associated construction costs. Analysis is presented in the Results section.

Table A.5
Correlations used for calculating the CAPEX. $C_{TES} = C_{HP\text{-}PB} + C_{LP\text{-}PB}$ (see Eqs. (10) and (11)). The exponents c,exp and t,exp are taken as 0.7.

Component	Correlation	Refs.
Land and site	$C_{land} = c_{land} \cdot A_{land}$; $C_{site} = c_{site} \cdot A_{site}$	[33,51]
Piping	$C_{piping} = f_{piping} \cdot C_{all,components}$	[33,51]
Axial compressor	$C_{LPC} = c_{comp}\dot{m}_{flow,ref}\left(\frac{\dot{m}_{flow}}{\dot{m}_{flow,ref}}\right)^{c,exp} r_{p,ref}\log(r_p) f_c$	[33,51,52]
Centrifugal compressor	$C_{LPC/HPC} = e^{9.1553+0.63\log(P_c/0.7457)} \cdot C_{rate,\$}$	[53]
Axial turbine	$C_{LPT/HPT} = c_{turb}\dot{m}_{flow,ref}\left(\frac{\dot{m}_{flow}}{\dot{m}_{flow,ref}}\right)^{t,exp} r_{p,ref}\log(r_p) f_t f_{T,turb}$	[33,51,52]
Generator	$C_{generator} = C_{gen,ref} \cdot W_{gen}^{0.5463}$	[33,51]
HP- and LP-PBs	$C_{TES} = c_{material} \cdot V_{TES} + C_{tank} + f_{T,TES} \cdot (c_{HT,ins} \cdot V_{HT,ins} + c_{LT,ins} \cdot V_{LT,ins} + c_{tank} \cdot V_{tank})$	[33,51]
PBs' tanks (pressure vessel)	$C_{tank} = (F_M C_v + C_{PL}) \cdot C_{rate,\$}$	[53]
Heat exchanger	$C_{HE} = 2835 \cdot (10.764 \cdot A_{HE})^{0.4} \cdot C_{rate,\$}$	[53]

Table A.6
Economic data considered. The exchange \$/€ applied was 1/0.86.

TES			
High-T insulation	Low-T insulation	Tank material	Foundations
$c_{HT,ins}$ [€/m^3]	$c_{LT,ins}$ [€/m^3]	c_{tank} [€/m^3]	$c_{foundations}$ [€/m^2]
4303	621	42 693	1220
Compressor			
Ref. cost	Ref. mass flux	Ref. r_p	
c_{comp} [€/(kg/s)]	$\dot{m}_{flow,ref}$ [kg/s]	$r_{p,ref}$ [–]	
23.3	515	15	
Turbine			
Ref. cost	Ref. mass flux	Ref. r_p	
c_{turb} [€/(kg/s)]	$\dot{m}_{flow,ref}$ [kg/s]	$r_{p,ref}$ [–]	
10.4	460	15	
Other components			
Generator	Piping		
$C_{gen,ref}$ [k€/MW$^{0.5463}$]	f_{piping} [–]		
92	0.15		
Other CAPEX costs			
Land	Site	Contingency	EPC
c_{land} [€/m^2]	c_{site} [€/m^2]	f_{CONT} [%]	f_{EPC} [%]
2.1	8.4	7	13
OPEX			
O&M fix	O&M variable	BOP	Electricity
$C_{OM,fix}$ [€/kW-yr]	$C_{OM,prod}$ [€/MWh-yr]	c_{BOP} [€/kW]	C_{el} [€/MWh]
9.98·$C_{rate,\$}$	1.33 ·$C_{rate,\$}$	43·$C_{rate,\$}$	50

Table A.7
C_{cavern} of lined-rock caverns. Cavern's volume: $V = 56.793 \cdot 10^3$ m^3 [42].

	Lined-rock cavern	
	Unbuilt [mill. €]	Built [mill. €]
Mining costs		
Waste rock disposal	1.2	–
Equipment	3.44	–
Supplies	4.3	–
Labor	6.6	–
Total	15.5	–
Commissioning costs		
Total	4.5	4.5
Total ($V = 56.793 \cdot 10^3$ m^3)	20	4.5
Extrapolation ($V = 3 \cdot 10^5$ m^3)	106	23.8

Table A.8
C_{cavern} of salt caverns for a volume: $V = 81.090 \cdot 10^3$ m^3 [42].

	Salt cavern	
	Unbuilt [mill. €]	Built [mill. €]
Drill and casing cost	2.4	–
Wate, fuel, pumping equipment and labor	1.6	–
Mechanical integrity costs	1.0	1.0
Brine disposal cost	2.0	–
Cost of brine transport	1.8	–
Total ($V = 81.09 \cdot 10^3$ m^3)	8.8	1.0
Extrapolation ($V = 3 \cdot 10^5$ m^3)	32.5	3.7

A.4. Correlations for the form of the Pareto fronts in terms of CAPEX

Correlations for the Pareto fronts in terms of the price of the purchased electricity. It is considered a compression train with two centrifugal compressors and copper slags in the packed-beds. C_{el} (€/MWh) represents the price at which electricity is bought during charge and the CAPEX (mill. €) is the total initial investment.

- Unbuilt salt cavern.

$$\begin{aligned} LCoS\,[€/\text{MWh}] =& 708983 + 7297.2 \cdot CAPEX - 35.0956 \cdot CAPEX^2 \\ &+ 0.0748906 \cdot CAPEX^3 + 89.0067 \cdot C_{el} \\ &- 2.49215 \cdot CAPEX \cdot C_{el} + 0.0235548 \cdot CAPEX^2 \cdot C_{el} \\ &- 7.40804 \times 10^{-5} \cdot CAPEX^3 \cdot C_{el} \\ &- 252460.0 \cdot \log(CAPEX). \end{aligned} \tag{25}$$

$$\text{This correlation applies for:} \quad \begin{aligned} &92 \le \text{CAPEX} \le 116 \text{ (mill.€)} \\ &0 \le C_{el} \le 100 \text{ (€/MWh).} \end{aligned} \tag{26}$$

- Built salt cavern.

$$\begin{aligned} LCoS[€/\text{MWh}] =& 87016.2 + 1624.55 \cdot CAPEX - 12.0018 \cdot CAPEX^2 \\ &+ 0.0393332 \cdot CAPEX^3 + 20.1168 \cdot C_{el} \\ &- 0.82821 \cdot CAPEX \cdot C_{el} + 0.0121382 \cdot CAPEX^2 \cdot C_{el} \\ &- 5.94013 \times 10^{-5} \cdot CAPEX^3 \cdot C_{el} \\ &- 36578.8 \cdot \log(CAPEX). \end{aligned} \tag{27}$$

$$\text{Correlation valid for:} \quad \begin{aligned} &60 \le \text{CAPEX} \le 75 \text{ (mill.€)} \\ &0 \le C_{el} \le 100 \text{ (€/MWh).} \end{aligned} \tag{28}$$

Table A.9
Properties of sensible (top) and PCM (bottom) materials used in PBs. The costs associated to the transport of the materials are not considered. All void fractions (ϵ) are equal to 0.39. Thermal emissivities are disregarded because of the temperatures considered. For alumina beads: $c_p(T) = -0.0022\,T^2 + 3.064\,T + 65.5464$ and $K(T) = 0.0001\,T^2 - 0.1773\,T + 79.925$, with temperatures in K.

Material	Density [kg/m^3]	Heat capacity [J/(kg K)]	Conductivity [W/(m K)]	$d_{p,in}/d_{p,out}$ [cm]	$c_{material}$ [€/kg]
Commercial ceramic [59]	2096	820	3.0	5/10	0.344
Alumina beads [65]	3550	$c_p(T)$	$K(T)$	5/10	0.30
Copper slags [46]	3600	1330	1.0	5/10	0.00
Steel slags [46]	3500	950	1.5	5/10	0.00
Magnetite [32]	5080	851	4.91	5/10	0.43
Quartzite [32]	2500	830	3.16	5/10	0.03
Basalt [32]	2640	1230	1.50	5/10	0.10
Adipic acid (PCM) [61,66]	1360 (solid) 1093 (liquid)	1590 (solid) 2260 (liquid) $\lambda_{fusion} = 2.73 \cdot 10^5$ J/kg $T_{fusion} = 150$–152 °C	0.15	5/10	8.6
Solar salt (PCM) [63,67]	1920	2300-1420 (solid–liquid) $\lambda_{fusion} = 2.50 \cdot 10^5$ J/kg $T_{fusion} = 185.7$ °C	0.24	5/10	0.645
Pentaerythritol (PCM) [62]	1161	2910-2980 (solid–solid) $\lambda_{phase} = 1.09 \cdot 10^5$ J/kg $T_{phase} = 227$–230 °C	0.387	5/10	2.32

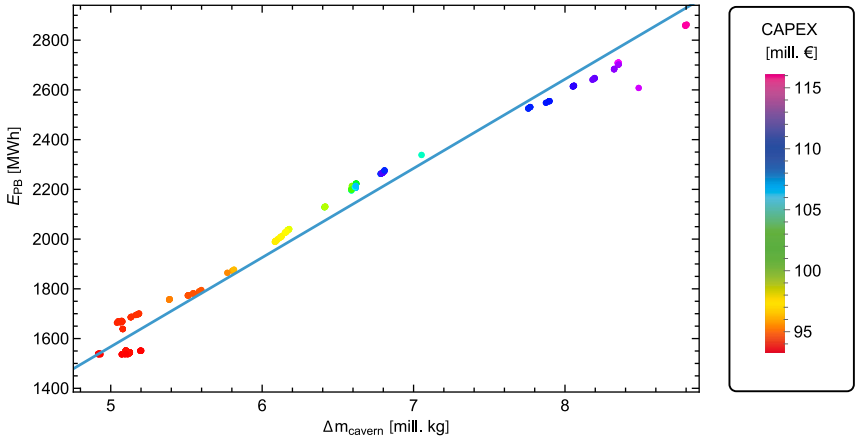

Fig. 22. Correlation between the energy stored in the PBs, E_{PB}, and the mass in the cavern, Δm_{cavern}, in terms of the CAPEX for the points in the Pareto front (see the particular conditions in the text).

A.5. Relationship between the mass in the cavern and the size of the thermal storages

In order to investigate the correlation among the energy stored in the PBs (E_{PB}), the mass contained in the high-pressure reservoir (Δm_{cavern}), and the CAPEX, the following relations are considered. First, the energy stored in both PB thermal storages can be expressed as:

$$E_{PB} = 2\pi(r_{out} - r_{in})H(1-\epsilon)\rho c_p(\Delta T_{LP\text{-}PB} + \Delta T_{HP\text{-}PB}), \tag{29}$$

and the total mass of air in the cavern (considering the air as an ideal gas) is:

$$\Delta m_{cavern} = (p_{max} - p_{min})V_{cavern}M/(R\overline{T}_{cavern}), \tag{30}$$

where $\overline{T}_{cavern}$ is the mean temperature in the reservoir.

Thus, it is possible to calculate both quantities for the points in the Pareto front and classify them in terms of the CAPEX. This is done in Fig. 22. The material in the PBs is copper slags, the compression train is formed by two centrifugal compressors, and the cavern is considered unbuilt. The figure shows that the relationship between E_{PB} and Δm_{cavern} is approximately linear, and that CAPEX increases with larger systems. Approximately, the fitting leads to:

$$E_{PB} = -225.75 + 358.589\,\Delta m_{cavern}, \tag{31}$$

with E_{PB} in MWh and Δm_{cavern} in mill. kg.

Appendix B. Multiobjective optimization

This Appendix presents the implementation of the NSGA II algorithm.

1. A set of initial variables: $x^1, x^2, \ldots, x^n$ in the decision space is randomly obtained. These points are mapped to the functions f^1 and f^2 in the optimization space, which are the two main key performance indicators used for the optimization. In this paper, $x^1, x^2, \ldots, x^n$ are equal to the initial variables (see Table 1), while f^1 and f^2 are equal to $LCoS$ and $CAPEX$.
2. Ordering by dominance: points in the optimization space are sorted according to the concept of dominance, the non-dominated points comprise front 1, and these points are subtracted. A new non-dominated set of points forms a second front, and so on.
3. Crowding distance: The crowding distance is calculated for each point of each front. First, the points of each front are sorted, and the extremal values (first and last) are assigned the value infinity to maintain diversity and extend the front. The crowding distance is calculated from the distance function

$$d_n = \frac{|f^1_{n+1} - f^1_{n-1}|}{f^1_{max} - f^1_{min}} + \frac{|f^2_{n+1} - f^2_{n-1}|}{f^2_{max} - f^2_{min}}, \tag{32}$$

which is computed for each point in the decision space.

4. Binary tournament selection: with this function, only the most valuable parents are selected to generate the offspring. It works as follows: two random parents are selected, and they compete in the front order. The winners comprise the front with less range. If they are in the same front, the winner is the parent with the greater crowding distance, which favors diversity. This step is repeated twice until the winner population is twice the fixed population (500 points). Each parent plays only 2 times in the tournament.
5. Simulated binary crossover to obtain the offspring: Two offsprings, h_1 and h_2, in the decision space are obtained from the two parents, p_1 and p_2,

$$\begin{aligned} h_1 &= \frac{1}{2}\left((1-\beta)p_1 + (1+\beta)p_2\right) \\ h_2 &= \frac{1}{2}\left((1+\beta)p_1 + (1-\beta)p_2\right), \end{aligned} \tag{33}$$

where $p_i = x_i^1, x_i^2, \ldots, x_i^n$ is the set of initial variables for each parent $i = 1, 2$. And β is defined as follows using a random number, u, with a value between 0 and 1,

$$\begin{aligned} &\text{If } \; u \leq 0.5 \rightarrow \beta = (2u)^{1/(\eta+1)} \\ &\text{If } \; u > 0.5 \rightarrow \beta = \left(\frac{1}{2(1-u)}\right)^{1/(\eta+1)}, \end{aligned} \tag{34}$$

where η is any non-negative real number, typically chosen between 2 and 5. Note that the first definition of β, i.e., when $u \leq 0.5$, is a contraction probability density-offspring decision variables are between parents' decision variables. The second definition of β is an expansion probability density-offspring decision variables are out of the range between the parents' decision variables.

After h_1 and h_2 are obtained, a random number between 0 and 1 is generated. If this number is smaller than the mutation probability $m_p = 0.15$, a polynomial mutation is applied on one offspring:

6. Polynomial mutation: A third offspring, h_3 with a mutation factor, δk, is obtained using a random number, r, ranging between 0 and 1,

$$\begin{aligned} &If \; r \leq 0.5 \rightarrow \delta k = (2r)^{1/(\eta_r+1)} - 1 \\ &If \; r > 0.5 \rightarrow \delta k = 1 - (2(1-r))^{1/(\eta_r+1)}, \end{aligned} \tag{35}$$

where η_r is the mutation distribution index, typical value of 5. In this way,

$$h_3 = h2 + \Delta x \cdot \delta k, \tag{36}$$

where $\Delta x = x_{max} - x_{min}$ of the set h_2. After that, $h_{1,2,3}$ are checked to fulfill the bounds and constraints.
7. Population update: The total population of the current generation, i.e., parents plus offsprings ($p + h$) are sorted by non-dominated fronts in the optimization space. The fixed number of offspring population (250 in this case) is selected from the first fronts to ensure elitism; it may occur that the total population belonging to the first Pareto fronts exceeds the predefined population size (250). In this case, individuals from the last accepted front are selected based on their crowding distance until the population size of 250 individuals is reached. Individuals with high crowding distance are selected, this ensures high variability and diversity in the population. The cycle is repeated for the next generation.

This iterative process continues until convergence is achieved, which is assessed via the stabilization of the Kullback–Leibler divergence (KLD). For each generation i, the round-trip efficiency (RTE) is used to compute the probability distribution, P_i(RTE). After multiple iterations, this distribution converges to the true Pareto front. The Kullback–Leibler divergence between successive generations, $i-1$ and i, is computed as follows,

$$\text{KLD} = \sum_n P_i(\text{RTE}), \log\left(\frac{P_i(\text{RTE})}{P_{i-1}(\text{RTE})}\right), \tag{37}$$

and this is used to measure the relative information between generations and ultimately, to establish the convergence of the algorithm. Once the KLD falls below a threshold, the distribution is considered sufficiently close to the true Pareto front, and additional iterations contribute only marginally to the identification of new points. In the present analysis the relative entropy from generation 150 to 204 exhibited decreasing values around 10^{-4} with small fluctuations between generations.

Data availability

Data will be made available on request.

References

[1] European Council, The 2030 climate and energy framework, 2017, https://www.consilium.europa.eu/en/policies/climate-change/2030-climate-and-energy-framework/.

[2] International Energy Agency, World energy investment 2024, 2024, https://www.iea.org/reports/world-energy-investment-2024.

[3] United Nations, Sustainable development goals, 2015, https://www.un.org/sustainabledevelopment/.

[4] C. Hunter, M.M. Penev, E.P. Reznicek, J. Eichman, N. Rustagi, S.F. Baldwin, Techno-economic analysis of long-duration energy storage and flexible power generation technologies to support high-variable renewable energy grids, Joule 5 (2021) 2077–2101, http://dx.doi.org/10.1016/j.joule.2021.06.018.

[5] F. Cebulla, T. Naegler, M. Pohl, Electrical energy storage in highly renewable european energy systems: Capacity requirements, spatial distribution, and storage dispatch, J. Ener. Storage 14 (2017) 211–213.

[6] M. Arbabzadeh, R. Sioshansi, J.X. Johnson, G.A. Keoelian, The role of energy storage in deep decarbonizationof electricity production, Nat. Commun. 10 (2019) 3413, http://dx.doi.org/10.1038/s41467-019-11161-5.

[7] T. Levin, J. Bistline, R. Sioshansi, W.J. Cole, J. Kwon, S.P. Burger, G.W. Crabtree, J.D. Denkins, R. O'Neil, M. Korpas, S. Wogrin, B.F. Hobbs, R. Rosner, V. Srinivasan, A. Botterud, Energy storage solutions to decarbonizeelectricity through enhanced capacity expansion modelling, Nat. Energy 8 (2023) 1199–1208, http://dx.doi.org/10.1038/s41560-023-01340-6.

[8] J.A. Dowling, K.Z. Rinaldi, T.H. Ruggles, S.J. Davis, M. Yuan, F. Tong, N.S. Lewis, K. Caldeira, Role of long-duration energy storage in variable renewable electricity systems, Joule 4 (2020) 1907–1928, http://dx.doi.org/10.1016/j.joule.2020.07.007.

[9] E. Barbour, D.L. Pottie, Adiabatic compressed air energy storage technology, Joule 5 (2021) 1914–1920.

[10] J. Bai, W. Wei, L. Chen, S. Mei, Modeling and dispatch of advanced adiabatic compressed air energy storage under wide operating range in distribution systems with renewable generation, Energy 206 (2020) 118051, http://dx.doi.org/10.1016/j.energy.2020.118051.

[11] Z. Tong, Z. Cheng, S. Tong, A review on the development of compressed air energy storage in china:technical and economic challenges to commercialization, Renew. Sust. Ener. Rev. 135 (2021) 110178, http://dx.doi.org/10.1016/j.rser.2020.110178.

[12] G. Li, L. Chen, X. Xue, Z. Guo, G. Wang, N. Xie, S. Mei, Multi-mode optimal operation of advanced adiabatic compressed air energy storage: Explore its value with condenser operation, Energy 248 (2022) 123600, http://dx.doi.org/10.1016/j.energy.2022.123600.

[13] M. King, A. Jain, R. Bhakar, J. Mathur, J. Wang, Overview of current compressed air energy storage projects and analysis ofthe potential underground storage capacity in india and the UK, Renew. Sust. Ener. Rev. 139 (2021) 110705, http://dx.doi.org/10.1016/j.rser.2021.110705.

[14] N. Georgousis, J. Diriken, M. Speetjens, C. Rindt, Comprehensive review on packed-bed sensible heat storage systems, J. Ener. Storage 121 (2025) 116516, http://dx.doi.org/10.1016/j.est.2025.116516.

[15] X. Yu, Z. Zhang, G. Qian, R. Jiang, L. Wang, R. Huang, Z. Li, Evaluation of PCM thermophysical properties on a compressed air energy storage system integrated with packed-bed latent thermal energy storage, J. Ener. Storage 81 (2024) 110519, http://dx.doi.org/10.1016/j.est.2024.110519.

[16] A. Alemam, S.N. Gunasekara, J.N. Chiu, A.I. Niedermeier, Investigation of hybrid sensible-latent packed bed thermal energy storage system, Appl. Therm. Eng. 279 (2025) 127375, http://dx.doi.org/10.1016/j.applthermaleng.2025.127375.

[17] R. Majumdar, S.K. Saha, Computational study of performance of cascaded multi-layered packed-bed thermal energy storage for high temperature applications, J. Ener. Storage 32 (2020) 101930, http://dx.doi.org/10.1016/j.est.2020.101930.
[18] S.B. Mousavi, M. Adib, M. Soltani, A.R. Razmi, Transient thermodynamic modeling and economic analysis of an adiabatic compressed air energy storage (A-CAES) based on cascade packed bed thermal energy storage with encapsulated phase change materials, Ener. Conv. Manag. 24 (2021) 114379, http://dx.doi.org/10.1016/j.enconman.2021.114379.
[19] G. Wei, G. Wang, C. Xu, X. Ju, L. Xing, X. Du, Y. Yang, Selection principles and thermophysical properties of high temperature phase change materials for thermal energy storage: A review, Renew. Sust. Ener. Rev. 81 (2018) 1771–1786, http://dx.doi.org/10.1016/j.rser.2017.05.271.
[20] L. Geissbühler, V. Becattini, G. Zanganeh, S. Zavattoni, M. Barbato, A. Haselbacher, A. Steinfeld, Pilot-scale demonstration of advanced adiabatic compressed air energystorage, part 1: Plant description and tests with sensible thermal-energy storage, J. Ener. Storage 17 (2018) 129–139, http://dx.doi.org/10.1016/j.est.2018.02.004.
[21] V. Becattini, L. Geissbühler, G. Zanganeh, A. Haselbacher, A. Steinfeld, Pilot-scale demonstration of advanced adiabatic compressed air energy storage, part 2: Tests with combined sensible/latent thermal-energy storage, J. Ener. Storage 17 (2018) 140–152.
[22] F. Lei, D. Korba, W. Huang, K. Randhir, L. Li, N. AuYeung, Thermochemical heat recuperation for compressed air energy storage, Ener. Conv. Manag. 250 (2021) 114889, http://dx.doi.org/10.1016/j.enconman.2021.114889.
[23] S. Wu, C. Zhou, E. Doroodchi, B. Moghtaderi, Thermodynamic analysis of a novel hybrid thermochemical-compressed air energy storage system powered by wind, solar and/or off-peak electricity, Ener. Conv. Manag. 180 (2019) 1268–1280, http://dx.doi.org/10.1016/j.enconman.2018.11.063.
[24] H. Yu, S. Engelkemier, E. Gençer, Process improvements and multi-objective optimization of compressed air energy storage (caes) system, J. Clean. Prod. 335 (2022) 130081.
[25] M.H. Mostafa, S.H.E. Abdel Aleem, S.G. Ali, Z.M. Ali, A.Y. Abdelaziz, Techno-economic assessment of energy storage systems using annualizedlife cycle cost of storage (LCCOS) and levelized cost of energy (LCOE) metrics, J. Ener. Storage 29 (2020) 101345, http://dx.doi.org/10.1016/j.est.2020.101345.
[26] Q. Zhou, Q. He, C. Lu, D. Du, Techno-economic analysis of advanced adiabatic compressed air energy storage system based on life cycle cost, J. Clean. Prod. 265 (2020) 121768, http://dx.doi.org/10.1016/j.jclepro.2020.121768.
[27] Y. Tian, T. Zhang, Z. Zhou, X. Zhang, Z. Wang, R. Chi, Z. Dong, Y. Lai, X. Xue, Comprehensive economic analysis of adiabatic compressed air energy storage system based on electricity spot market policy, J. Ener. Storage 103 (2024) 114333, http://dx.doi.org/10.1016/j.est.2024.114333.
[28] K. Deb, Multi-Objective Optimization using Evolutionary Algorithms, John Wiley & Sons, Inc, 2001.
[29] E.H. Güleryüz, D.N. Özen, Advanced exergy and exergo-economic analyses of an advanced adiabatic compressed air energy storage system, J. Ener. Storage 55 (2022) 105845, http://dx.doi.org/10.1016/j.est.2022.105845.
[30] A. Bagdanavicius, A. Masoud Ali, E.R. Barbour, M. Martins de Oliveira Junior, D.L. Pottie, S. Garvey, Z. Baniamerian, E. Hough, Exergoeconomic evaluation of adiabatic compressed air energy storage: Effects of pressure ratio and configuration, J. Ener. Storage 138 (2025) 118662, http://dx.doi.org/10.1016/j.est.2025.118662.
[31] E.H. Güleryüz, D.N. Özen, A.M. Acilar, Advanced exergy and exergo-economic analyses of an advanced adiabatic compressed air energy storage system, part 2: Parametric study and optimization, J. Ener. Storage 70 (2023) 107886, http://dx.doi.org/10.1016/j.est.2023.107886.
[32] M. Mersch, P. Sapin, A.V. Olympios, Y. Ding, N. Mac Dowell, C.N. Markides, A unified framework for the thermo-economic optimisation of compressed-air energy storage systems with solid and liquid thermal stores, Ener. Conv. Manag. 287 (2023) 117061.
[33] S. Guccione, R. Guedez, Techno-economic analysis of power-to-heat-to-power plants: Mapping optimal combinations of thermal energy storage and power cycles, Energy 312 (2024) 133500, http://dx.doi.org/10.1016/j.energy.2024.133500.
[34] Z. Baniamerian, S. Garvey, J. Rouse, B. Cardenas, D.L. Pottie, E.R. Barbour, A. Bagdanavicius, How pressure affects costs of power conversion machinery in compressed air energy storage; part i: Compressors and expanders, J. Ener. Storage 89 (2024) 111791, http://dx.doi.org/10.1016/j.est.2024.111791.
[35] Z. Baniamerian, S. Garvey, J. Rouse, B. Cardenas, D.L. Pottie, E.R. Barbour, A. Bagdanavicius, How pressure affects costs of power conversion machinery in compressedair energy storage; part II: Heat exchangers, J. Ener. Storage 86 (2024) 111138, http://dx.doi.org/10.1016/j.est.2024.111138.
[36] V. Viswanathan, K. Mongird, R. Franks, X. Li, V. Sprenkle, R. Baxter, 2022 Grid Energy Storagetechnology Cost and Performance Assessment, Tech. Rep. PNNL-33283, Pacific Northwest National Laboratory (PNNL), 2022, https://www.pnnl.gov/sites/default/files/media/file/ESGCCostPerformanceReport2022PNNL-33283.pdf.
[37] S. Ahmed, D.L. Flowers, P.J. Balducci, Technology Strategy Assessment Findings from Storage Innovations 2030. Compressed Air Energy Storage, Tech. Rep. DOE/OE-0037, US Department of Energy, 2023, https://www.energy.gov/oe/storage-innovations-2030.
[38] O. Schmidt, Projecting the future lifetime cost of electricity storage technologies, 2025, https://www.storage-lab.com/levelized-cost-of-storage?utm_source=chatgpt.com.
[39] A. Smallbone, V. Jülch, R. Wardle, A.P. Roskilly, Levelised cost of storage for pumped heat energy storage in comparison with other energy storage technologies, Ener. Conv. Manag. 152 (2017) 221–228, http://dx.doi.org/10.1016/j.enconman.2017.09.047.
[40] D. Pérez-Gallego, J. González-Ayala, A. Medina, I. Calderón-Vásquez, A. Calvo Hernández, Full dynamic simulation of an adiabatic compressed air energy storage plant with radial-flow packed-bed storage and an organic Rankine cycle unit, Ener. Conv. Manag. 348 (2026) 120764, http://dx.doi.org/10.1016/j.enconman.2025.120764.
[41] A. Giostri, E. Macchi, An advanced solution to boost sun-to-electricity efficiency of parabolic dish, Sol. Ener. 139 (2016) 337–354.
[42] D.D. Papadias, R.K. Ahluwalia, Bulk storage of hydrogen, Int. J. Hydrog. Energy 46 (70) (2021) 34527–34541.
[43] M. Raju, S.K. Khaitan, Modeling and simulation of compressed air storage in caverns: A case studyof the huntorf plant, Appl. Energy 89 (2012) 474–481, http://dx.doi.org/10.1016/j.apenergy.2011.08.019.
[44] E. Barbour, Y. Mignard, M. amd Ding, Y. Li, Adiabatic compressed air energy storage with packed-bed thermal energy storage, Appl. Energy 155 (2015) 804–815, http://dx.doi.org/10.1016/j.apenergy.2015.06.019.
[45] H. Peng, Y. Yang, R. Li, X. Ling, Thermodynamic analysis of an improved adiabatic compressed air energy storage system, Appl. Energy 183 (2016) 1361–1373.
[46] S. Trevisan, R. Guedez, Design optimization of an innovative layered radial-flow high-temperature packed bed thermal energy storage, J. Ener. Storage 83 (2024) 110767, http://dx.doi.org/10.1016/j.est.2024.110767.
[47] J.D. McTigue, A.J. White, A comparison of radial-flow and axial-flow packed beds for thermal energy storage, Appl. Energy 227 (2017) 533–541, http://dx.doi.org/10.1016/j.apenergy.2017.08.179.
[48] D. Pérez-Gallego, J. González-Ayalaa, A. Medina, A. Calvo Hernández, Comprehensive review of dynamical simulation models of packed-bed systems for thermal energy storage applications in renewable power production, Heliyon 11 (2025) e42803, http://dx.doi.org/10.1016/j.heliyon.2025.e42803.
[49] A. Elouali, T. Kousksou, T. El Rhakifia, S. Hamdaoui, M. Mahdaoui, A. Allouhi, Y. Zeraouli, Physical models for packed bed: Sensible heat storage systems, J. Ener. Storage 23 (2019) 69–78, http://dx.doi.org/10.1016/j.est.2019.03.004.
[50] S. Ergun, A.A. Orning, Fluid flow through randomly packed columns and fluidized beds, Ind. Eng. Chem. 41 (6) (1949) 1179–1184.
[51] S. Guccione, R. Guedez, Techno-economic optimization of molten salt based CSP plants through integration of supercritical CO_2 cycles and hybridization with PV and electric heaters, Energy 283 (2023) 128528, http://dx.doi.org/10.1016/j.energy.2023.128528.
[52] J. Spelling, Hybrid Solar Gas-Turbine Power Plants, (Ph. D. thesis), KTH Royal Institute of Technology, Department of Energy Technology, Stockholm, Sweden, 2013.
[53] W.D. Seider, D.R. Lewin, J. Seader, S. Widagdo, R. Gani, K.M. Ng, Product and Process Design Principles: Synthesis, Analysis and Evaluation, John Wiley & Sons, 2016.
[54] V. Black, Cost and Performance Data for Power Generation Technologies, National Renewable Energy Laboratory (NREL), 2012, https://refman.energytransitionmodel.com/publications/1921.
[55] Y. Li, S. Liao, G. Liu, Thermo-economic multi-objective optimization for a solar-dish brayton system using NSGA-II and decision making, Elect. Power. Energ. Sys. 64 (2015) 167–175.
[56] A.B. Uday, N. Naik, G.M. Madhu, C. Vyjayanthi, C. Modi, Implementation and validation of NSGA-II algorithm for constrained and unconstrained multi-objective optimization problem, IEEE IAS Glob. Conf. Emerg. Technol. (2022) 539–544.
[57] F. Crotogino, K.U. Mohmeyer, R. Sharf, Huntorf CAES:more than 20 years of successful operation, in: Spring 2001 Meeting, Orlando, Florida, 2001, http://www.fze.uni-saarland.de/AKE_Archiv/AKE2003H/AKE2003H_Vortraege/AKE2003H03c_Crotogino_ea_HuntorfCAES_CompressedAirEnergyStorage.pdf.
[58] A. Sciacovelli, Y. Li, H. Chen, Y. Wu, J. Wang, S. Garvey, Y. Ding, Dynamic simulation of adiabatic compressed air energy storage (A-CAES) plant with integrated thermal storage - link between components performance and plant performance, Appl. Energy 185 (2017) 16–28, http://dx.doi.org/10.1016/j.apenergy.2016.10.058.
[59] S. Gobain, 2025. link.
[60] M. Ashmore, L. Katlego, L. Robert, O. Denis, N. Karidewa, Thermal stratification performance of a packed bed latent heat storage system during charging, in: E3S web of conferences, vol. 64, EDP Sciences, 2018, p. 03001.
[61] L. Seyitini, B. Belgasim, C.C. Enweremadu, Numerical investigation of a hybrid latent-sensible thermal energy storage system for low temperature industrial applications, J. Energy Storage 123 (2025) 116759.
[62] D. Bielsa, P. Arribalzaga, I. Martinez, M. Hashemi-Tilehnoee, I. Torrano, A. Serrano, E. Palomo del Barrio, Experimental and numerical study of a novel cost-effective macro-encapsulated solid–solid pcm for solar process heat thermal energy storage, Appl. Therm. Eng. 280 (2025) 128460, http://dx.doi.org/10.1016/j.applthermaleng.2025.128460.

[63] F.R. Martínez, E. Borri, M.S., S. Ushak, L.F. Cabeza, Phase change materials for thermal energy storage in industrial applications, Heliyon 11 (2025) e41025, http://dx.doi.org/10.1016/j.heliyon.2024.e41025.

[64] L. Cabeza P. Tagle-Salazar, C. Prieto, Performance benchmark of thermal energy storage concepts in concentrating solar power, Appl. Energy 404 (2026) 127183, http://dx.doi.org/10.1016/j.apenergy.2025.127183.

[65] M. Cascetta, G. Cau, P. Puddu, F. Serra, A comparison between CFD simulation and experimental investigation of a packed-bed thermal energy storage system, Appl. Therm. Eng. 98 (2016) 1263–1272.

[66] N. Snekha, V. Hari Suthan, K. Suganthi, S. Naren Raggavendra, S. Sudharsan, R. Aishwarya, K. Rajan, Zno-adipic acid composites as phase change material for latent heat thermal energy storage systems, Micro Nano Syst. Lett. 12 (1) (2024) 24.

[67] T. Ong, M. Sarvghad, S. Bell, G. Will, T. Steinberg, Y. Yin, G. Andersson, D. Lewis, Review on the challenges of salt phase change materials for energy storage in concentrated solar power facilities, Appl. Therm. Eng. 238 (2024) 122034, http://dx.doi.org/10.1016/j.applthermaleng.2023.122034.